

RESEARCH ARTICLE

Hypomorphic and hypermorphic mouse models of *Fsip2* indicate its dosage-dependent roles in sperm tail and acrosome formation

Xiang Fang^{*,1}, Yaser Gamallat^{*,1}, Zhiheng Chen², Hanran Mai³, Pei Zhou¹, Chuanbo Sun¹, Xiaoliang Li⁴, Hong Li¹, Shuxin Zheng¹, Caihua Liao¹, Miaomiao Yang¹, Yan Li¹, Zeyu Yang⁵, Caiqi Ma², Dingding Han¹, Liandong Zuo³, Wenming Xu⁴, Hao Hu^{1,6,7}, Ling Sun^{2,‡} and Na Li^{1,‡}

ABSTRACT

Loss-of-function mutations in multiple morphological abnormalities of the sperm flagella (MMAF)-associated genes lead to decreased sperm motility and impaired male fertility. As an MMAF gene, the function of fibrous sheath-interacting protein 2 (*FSIP2*) remains largely unknown. In this work, we identified a homozygous truncating mutation of *FSIP2* in an infertile patient. Accordingly, we constructed a knock-in (KI) mouse model with this mutation. In parallel, we established an *Fsip2* overexpression (OE) mouse model. Remarkably, KI mice presented with the typical MMAF phenotype, whereas OE mice showed no gross anomaly except for sperm tails with increased length. Single-cell RNA sequencing of the testes uncovered altered expression of genes related to sperm flagellum, acrosomal vesicle and spermatid development. We confirmed the expression of *Fsip2* at the acrosome and the physical interaction of this gene with *Acrv1*, an acrosomal marker. Proteomic analysis of the testes revealed changes in proteins sited at the fibrous sheath, mitochondrial sheath and acrosomal vesicle. We also pinpointed the crucial motifs of *Fsip2* that are evolutionarily conserved in species with internal fertilization. Thus, this work reveals the dosage-dependent roles of *Fsip2* in sperm tail and acrosome formation.

KEY WORDS: FSIP2, Male infertility, Sperm, MMAF, Mouse model

INTRODUCTION

Male infertility is a major issue in human reproductive health, affecting more than 20 million men worldwide and preventing natural conception (Niederberger, 2020; Visser et al., 2020). Asthenozoospermia, a symptom frequently observed in infertile men with less progressive motile sperm (Cooper et al., 2010), is

caused by morphological and functional defects of the sperm flagellum. A severe asthenozoospermia with near-zero progressive sperm, namely, multiple morphological abnormalities of the sperm flagella (MMAF), is characterized by sperm with absent, short, irregular and/or coiled flagella (Ben Khelifa et al., 2014; Yang et al., 2015). Thus far, defects in several flagellum-associated genes, including *DNAH1*, *CFAP43*, *CFAP44*, *SPEF2*, *QRICH2*, *ARMC2*, *CFAP58* and *AKAP4* (Ben Khelifa et al., 2014; Baccetti et al., 2005; Tang et al., 2017; Coutton et al., 2018; Coutton et al., 2019; Liu et al., 2019b; Shen et al., 2019; He et al., 2020), have been identified in patients with MMAF.

As an evolutionarily conserved organelle, the sperm tail or flagellum is an axoneme-based structure that exerts a significant impact on sperm motility and fertilization (Eddy et al., 2003; Lehti and Sironen, 2017). In mammals, the sperm tail is structurally divided into three major parts: the midpiece (MP), the principal piece and the end piece (Fawcett, 1975). The MP comprises the outer dense fibers (ODFs), the mitochondrial sheath and the microtubule-derived axoneme (Lehti and Sironen, 2017; Piasecka et al., 2001). The principal piece contains the fibrous sheath in place of the mitochondrial sheath (Lehti and Sironen, 2017; Brown et al., 2003). The end piece is composed of the axoneme surrounded by the plasma membrane, without any accessory structures.

The fibrous sheath is a unique cytoskeletal structure in the principal piece of the sperm flagellum, comprising two longitudinal columns connected by circumferential ribs and surrounded by outer dense fibers (Eddy et al., 2003; Eddy, 2007). The fibrous sheath provides the sperm tail with mechanical support that modulates flagellar bending and defines the shape of the flagellar beat (Ricci and Breed, 2005). In addition, the fibrous sheath also serves as a scaffold for glycolytic enzymes and signaling molecules involved in regulating sperm maturation, capacitation, motility, hyperactivation and/or the acrosome reaction (Eddy et al., 2003; Eddy, 2007).

The acrosome is a unique membrane-bound organelle that covers the anterior portion of the head of the mature spermatozoon (Hirohashi and Yanagimachi, 2018). It derives from the Golgi apparatus and contains digestive enzymes, which are indispensable for the acrosome reaction and successful fertilization (Khawar et al., 2019). ACRV1 is an acrosomal matrix protein that is evolutionarily conserved among mammals (Cruz et al., 2020). It is predominantly located in both round and elongated spermatids in the testes; a polyclonal antibody of *Acrv1* has been shown to be useful for staging the cycle of seminiferous epithelium in the mouse (Tang et al., 2012; Osuru et al., 2014). The lateral flow immunochromatographic assay of ACRV1 was recently implemented for the evaluation of male infertility (Bieniek et al., 2016).


Fibrous sheath-interacting protein 2 (FSIP2) is one of the largest proteins (6907 amino acids) in the human genome and a major component of the fibrous sheath (Brown et al., 2003). Six

¹Laboratory of Medical Systems Biology, Guangzhou Women and Children's Medical Center, Guangzhou Medical University, 510623 Guangzhou, China.

²Center of Reproductive Medicine, Guangzhou Women and Children's Medical Center, Guangzhou Medical University, 510623 Guangzhou, China. ³Department of Andrology, Guangzhou Women and Children's Medical Center, Guangzhou Medical University, 510623 Guangzhou, China. ⁴Key Laboratory of Obstetric, Gynecologic and Pediatric Diseases and Birth Defects of Ministry of Education, West China Second University Hospital, Sichuan University, 610041 Chengdu, China. ⁵Guangdong Technion—Israel Institute of Technology, Shantou, 515063 Guangdong, China. ⁶Third Affiliated Hospital of Zhengzhou University, 450052 Zhengzhou, China. ⁷Guangdong Provincial Key Laboratory of Research in Structural Birth Defect Disease, Guangzhou Women and Children's Medical Center, Guangzhou Medical University, 510623 Guangzhou, China.

*These authors contributed equally to this work

[‡]Authors for correspondence (sunling6299@163.com; lina@cougarlab.org)

 X.F., 0000-0001-6958-3775; Y.G., 0000-0001-9980-2107; Z.C., 0000-0002-9756-3816; C.M., 0000-0002-3178-9820; H.H., 0000-0002-3567-609X; L.S., 0000-0002-4267-8210; N.L., 0000-0001-6163-1648

homozygous loss-of-function mutations of *FSIP2* were recently reported, which could cause the typical human MMAF phenotypes (Martinez et al., 2018; Liu et al., 2019a). A completely disorganized fibrous sheath associated with axonemal defects was observed in all patients carrying *FSIP2* mutations, with abnormalities in fibrous sheath, microtubules and dynein arm-associated proteins (Martinez et al., 2018; Liu et al., 2019a). *FSIP2* is also reported to interact directly with AKAP4, the most abundant protein in the sperm fibrous sheath (Brown et al., 2003). However, the molecular mechanisms underlying the MMAF phenotypes caused by the mutations in *FSIP2* remain undiscovered.

In this study, we identified a novel homozygous truncating mutation of *FSIP2* in a patient with MMAF through whole-exome sequencing (WES). Based on this, we generated two transgenic mouse models: an *Fsip2*-knock-in (KI) mouse that mimics the truncation mutation, which displayed typical MMAF phenotypes; and an *Fsip2*-overexpression (OE) mouse, which exhibited longer sperm tails compared with wild-type (WT) mice. Truncation and overexpression of *Fsip2* reciprocally affected proteins associated with the fibrous sheath, mitochondrial sheath and acrosomal vesicle. Intriguingly, we showed that two C-terminal motifs of *Fsip2* were only conserved in species with internal fertilization. Thus, our results provide new insights into the roles of *Fsip2* in the sperm tail and acrosome formation.

RESULTS

A homozygous truncating mutation identified in *FSIP2* from a patient with MMAF

An infertile male patient who presented with primary infertility and normal sexual function was enrolled in our study. The analysis of three semen samples over 3 months showed normal semen volume, pH and concentration, but progressive motility was remarkably impaired (Table 1). Scanning electron microscopy (SEM) identified the MMAF phenotypes of the spermatozoa: short tails, thin principal pieces and abnormal MPs (Fig. 1A). Aberrant sperm ultrastructures were further confirmed by transmission electron microscopy (TEM): the mitochondrial sheath was dysplastic and disorganized, and the fibrous sheath was absent (Fig. 1B). In order to uncover the genetic cause of the MMAF phenotypes, we performed WES and found a homozygous 1 base pair (bp) insertion in *FSIP2*. A premature stop codon downstream of the 2790th residue was introduced by the c.8368_8369insC mutation, which was further confirmed by Sanger sequencing (Fig. 1C). This mutation was not found in the following sequence databases: dbSNP (<https://www.ncbi.nlm.nih.gov/snp/>); 1000 Genomes Project (<https://www.internationalgenome.org/>); ExAC (exac.broadinstitute.org/); or gnomAD (<https://gnomad.broadinstitute.org/>).

Table 1. Seminal parameters of the patient with MMAF

Parameter	Sample number*		
	#1	#2	#3
Volume (ml)	3.5	3.0	2.5
Concentration (10 ⁶ /ml)	44.9	143.8	47.5
pH	7	7	7
Total motility (%)	37.17	10.8	8.9
Progressive motility (%)	8.63	1.5	1.2
Morphology (%) [‡]	4	2	1
Viability (%) [§]	45	48	45

*The analyses were repeated three times in 3 months (indicated by #1, #2 and #3, respectively).

[‡]According to Kruger criteria.

[§]These values were determined after the hypo-osmotic swelling testing (HOST).

Evaluation of *Fsip2*-KI and *Fsip2*-OE mouse models

To mimic the mutation (c.8368_8369insC, p.2790fs) in *FSIP2* found in the patient with MMAF and to evaluate the effects of *Fsip2* overexpression, we generated the *Fsip2*-KI and *Fsip2*-OE mouse models. Sanger sequencing confirmed the insertion mutation (c.8137insC) located in the 16th exon of *Fsip2* in the *Fsip2*-KI mice (Fig. 2A). We detected substantially reduced and increased mRNA expression levels of *Fsip2* in KI and OE mice, respectively (Fig. 2B). The *Fsip2* copy numbers of OE mice were at least 4.5-fold higher than those of WT mice and 70% of OE mice showed commensurately increased *Fsip2* mRNA levels (Fig. 2C). Female homozygous KI mice were fertile, whereas male homozygous KI mice were sterile despite showing normal mating behavior with successful ejaculations and vaginal plug formation. By contrast, both the female and male OE mice were fertile and there was no significant difference in the testes weights of WT, KI or OE mice (Table S1). Sperm from WT, KI and OE mice were then extracted and analyzed with a computer-assisted sperm analysis (CASA) system. Compared with WT mice, the viability and motility of sperm from KI mice were significantly attenuated (Table 2). However, we observed no obvious differences in sperm viability or motility between WT and OE mice (Table 2).

The immunostaining results confirmed the absence of *Fsip2* in the sperm from KI mice (Fig. 2D; Fig. S1). It was also noteworthy that *Fsip2* was not only localized to the principal piece, but also found in the MP and the head of the sperm in WT and OE mice (Fig. 2D). This observation suggested that the existence and functionality of *Fsip2* are not only restricted to the fibrous sheath.

More spermatozoa could be observed in the seminiferous tubules of OE mice (Fig. 2E). The sperm flagella of KI mice were short, curved and frayed (Fig. 2F), consistent with the morphology of the sperm from the patient with MMAF. SEM and TEM further revealed the MMAF phenotypes and corresponding ultrastructural defects of KI-mice sperm: the flagella were short, the fibrous sheaths were absent and the axonemes were exposed (Fig. 2G,H). We did not observe any structural alterations in the flagella when we compared OE and WT sperm.

Flagella of OE-mice sperm show longer principal pieces and MPs relative to those of WT mice

Diff-Quick staining revealed some longer spermatozoa from OE mice (Fig. 3A). To determine the lengths of the sperm tails, MitoTrack signal (red) and Akap4 immunostaining (green) were used to indicate the MPs and principal pieces, respectively (Fig. 3B). Our results revealed that both principal pieces and MPs of sperm from OE mice were significantly longer than those from WT mice (Fig. 3C; $P < 0.01$). The sum of the average lengths of the principal pieces and MPs of WT-mice sperm was $115.21 \pm 3.09 \mu\text{m}$. If the sum of the lengths of the principal piece and MPs of an OE-mouse sperm was greater than $124.48 \mu\text{m}$ [$115.21 + (3 \times 3.09)$], the sperm was defined as a 'super-long' sperm. According to this definition, there were 7.4 times more 'super-long' sperm in OE mice compared with WT mice.

Overexpression of *Fsip2* causes global changes in the testicular gene expression profile

To explore the alterations in the gene expression profile of the testis when induced by the mutation or overexpression of *Fsip2*, the testes of WT, KI and OE mice were processed and analyzed in a pipeline of 10x Genomics single-cell RNA sequencing (RNA-seq). We captured 39,502 cells and partitioned them into

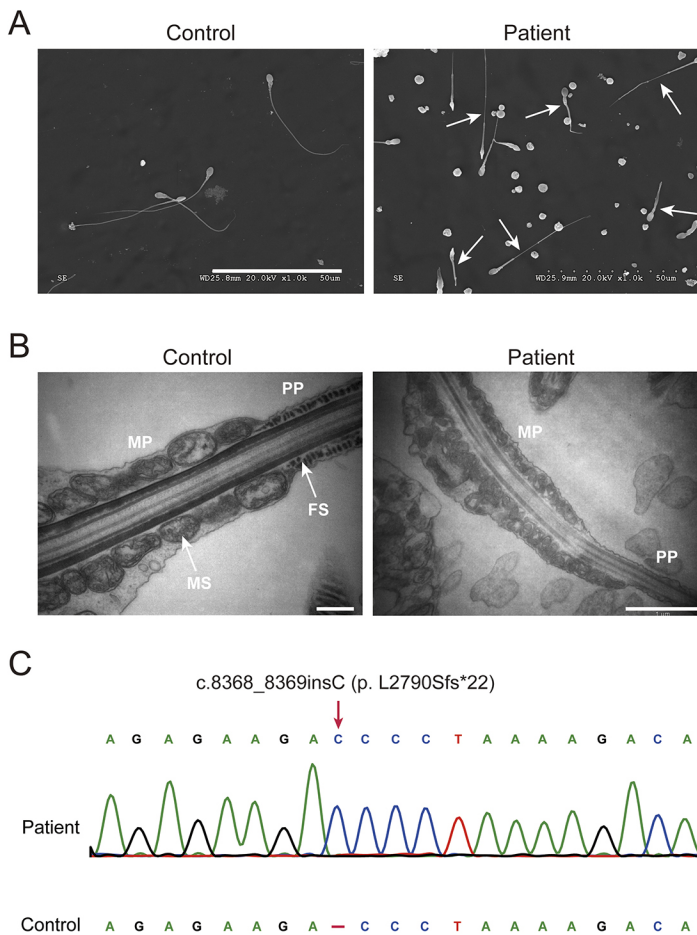


Fig. 1. Morphology and ultrastructure of sperm from the patient with MMAF. (A) SEM images showing sperm morphology from a normal control and the patient. White arrows indicate the sperm with MMAF phenotypes. (B) TEM images of the junctional region between the MP and the principal piece of the sperm tail of a normal control and the patient. (C) Electropherogram of Sanger sequencing confirmed a 1 bp insertion of *FSIP2* (pink arrow). Scale bars: 50 μ m in A; 0.5 μ m and 1 μ m, for the left and right images, respectively in B. FS, fibrous sheath; MS, mitochondrial sheath; PP, principal piece.

14 clusters, which were then classified into six cell types (spermatogonia, spermatocytes, round spermatids, elongating spermatids, Sertoli cells and Leydig cells) according to previously defined marker genes (Green et al., 2018) (Fig. 4A). *Fsip2* was expressed in all cell types and significantly enriched in round spermatids (Fig. 4B).

The round spermatid cluster was then further subdivided into four subclusters (Round spermatid 1, 2, 3 and 4; Fig. 4C), corresponding to the four stages of round spermatids (RS2, RS4, RS6 and RS8, respectively) proposed recently (Chen et al., 2018). We observed no obvious differences between the cell proportions of the four stages of round spermatids from WT and KI mice; however, the proportion of round spermatid 2 in OE mice was substantially higher than in WT and KI mice (Fig. 4D). The marker genes of round spermatid 2 included *Acrv1*, *Spaca1* and *Spaca3*, which were indispensable for acrosome formation.

We identified the differentially expressed genes between round spermatids of OE and WT mice. Round spermatid 1 consisted of 156 upregulated and 101 downregulated genes; round spermatid 2 consisted of 512 upregulated and 599 downregulated genes; round spermatid 3 consisted of 365 upregulated and 261 downregulated genes; and round spermatid 4 consisted of 622 upregulated and 440 downregulated genes. *Fsip2* was upregulated in all subclusters of round spermatids. Gene Ontology (GO) enrichment analysis indicated that the upregulated genes of round spermatids 1, 2, 3 and 4 of OE mice were involved in sperm flagellum and motile cilium (Fig. 4E), in agreement with the longer principal pieces and MPs observed in the sperm from OE mice (Fig. 3C). In addition, the upregulated genes were also significantly enriched in the GO terms

of acrosomal vesicle, spermatid development and spermatid differentiation (Fig. 4E).

By contrast, we found far fewer differentially expressed genes among the four subclusters of round spermatids of KI and WT mice, comprising 13 (0 upregulated and 13 downregulated), 40 (17 upregulated and 23 downregulated), five (two upregulated and three downregulated) and six (two upregulated and four downregulated) genes, respectively. The top three downregulated genes for the four subclusters of round spermatids are summarized in Table S2. *Fsip2* was downregulated in all subclusters of round spermatids. In addition, the top downregulated genes in KI mice included *Tcte3* (*Dynlt2a1*), *Tuba3b* and *Slx11*, which were primarily expressed in spermatocytes and round spermatids (Fig. 4F). Three uncharacterized genes, *1700017L05Rik*, *1700109H08Rik* and *Gm36368* (mainly expressed in round spermatids), were also downregulated (Fig. 4F).

Fsip2 interacts with the acrosomal protein Acrv1

As mentioned above, *Fsip2* was expressed in the sperm head (Fig. 2E); single-cell RNA-seq analysis indicated that the upregulated genes in round spermatids of OE mice were also enriched in the acrosomal vesicle (Fig. 4E). Our immunostaining results showed that, in the acrosome, *Fsip2* was co-expressed with *Acrv1*, a known acrosomal marker (Fig. 5A). The Duolink Proximity Ligation Assay (PLA) further confirmed the interaction between *Fsip2* and *Acrv1* in the acrosome, because a red PLA signal was observed (Fig. 5B,C). In addition, expression of *Acrv1* was significantly increased in OE mice compared with WT mice, whereas diminished expression of *Acrv1* was observed in KI mice (Fig. 5D,E).

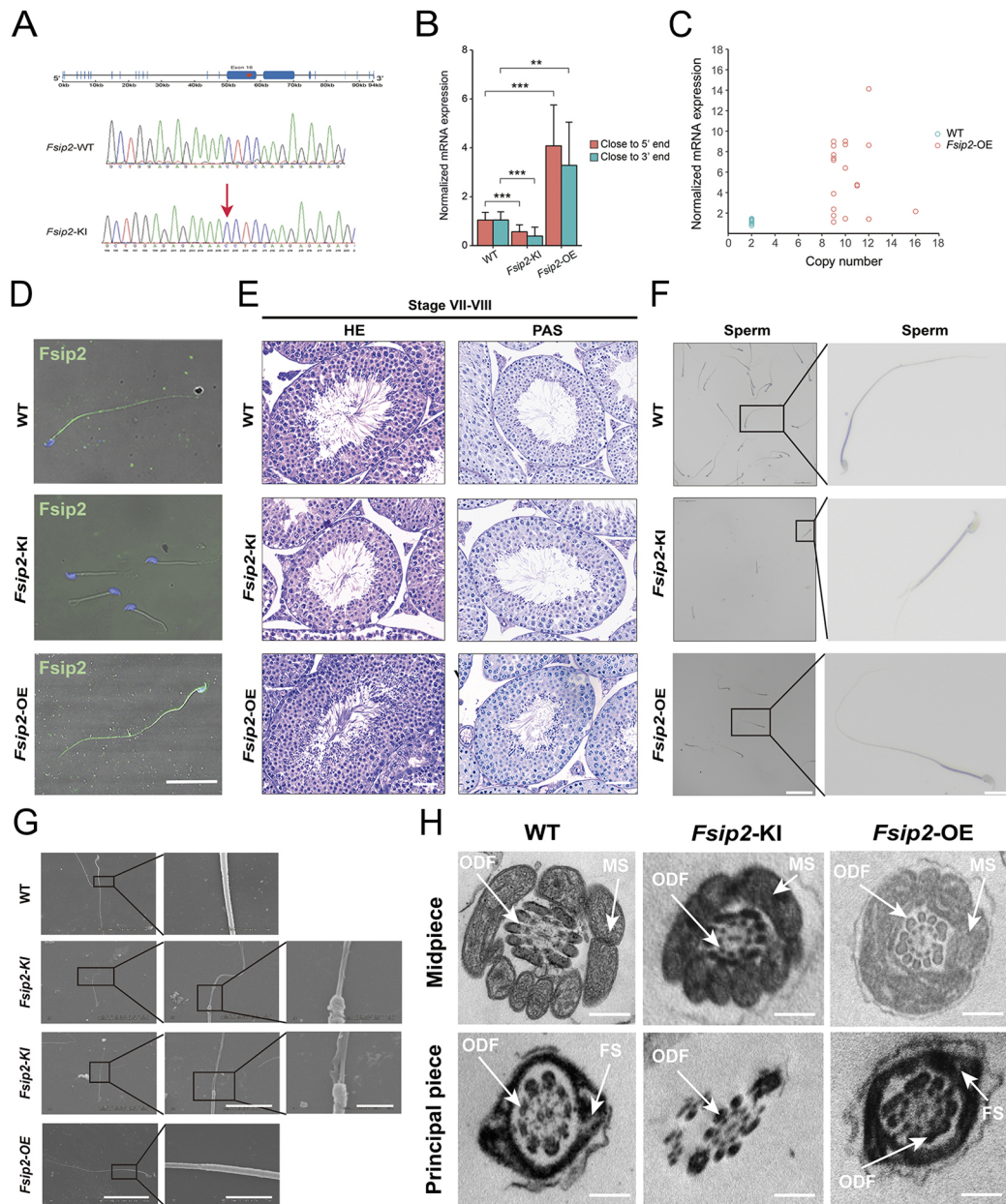


Fig. 2. The *Fsip2*-KI mouse model has spermatozoa with MMAF phenotypes. (A) Schematic of the mutation site (red star) of the *Fsip2*-KI mice, and Sanger sequencing confirming a 1 bp insertion (c.8137insC; pink arrow) of *Fsip2*. (B) Real-time qPCR results of the normalized mRNA expression levels of *Fsip2* in WT, KI and OE mice. *Gapdh* was used as the reference. Data are mean \pm s.d. $n=4$, 10 and 4 for WT, KI and OE mice, respectively. P -values were calculated using the two-tailed t -test. ** $P<0.01$, *** $P<0.001$. (C) Bubble plot representing the copy number and corresponding normalized mRNA level of *Fsip2* in OE mice. $n=10$ and 19 for WT and OE mice, respectively. (D) Immunostaining of *Fsip2* (green) in the cauda epididymal spermatozoa in WT, KI and OE mice. The nuclear marker DAPI is in blue, merged with differential interference contrast (DIC) (gray). (E) Morphological assessment of testicular tissues using Hematoxylin and Eosin (HE) and Periodic-Acid Schiff (PAS) staining of stage VII-VIII seminiferous tubules in WT (top), KI (middle) and OE (bottom) mice. (F) Papanicolaou (BASO) staining of cauda epididymal spermatozoa and corresponding magnified views in WT (top), KI (middle) and OE (bottom) mice. (G) SEM of cauda epididymal spermatozoa in WT (top), KI (middle) and OE (bottom) mice. (H) TEM showing ultrastructure of the MPs (top) and principal pieces (bottom) in WT (left), KI (middle) and OE (right) mice. Scale bars: 200 nm in H; 2 μ m in G (right panel); 5 μ m in G (middle panel, the two middle images); 10 μ m in F (magnified image) and G (middle panel, the top and bottom images), 25 μ m in D; 50 μ m in E, G (left panel); 100 μ m in F. FS, fibrous sheath; MS, mitochondrial sheath; ODF, outer dense fibers.

Dosage alteration of *Fsip2* affects proteins associated with the fibrous sheath, mitochondrial sheath and acrosomal vesicle

To reveal the impacts of truncation and overexpression of *Fsip2* on protein expression in the testis, we investigated protein expression levels in the testes of WT, KI and OE mice using a proteomics approach. We quantified a total of 6693 proteins from KI mice, of which 656 were identified to be expressed differentially compared

with WT mice, including 107 downregulated proteins and 549 upregulated proteins (Fig. 6A). In terms of OE mice, a total of 7342 proteins were quantified, of which 87 were identified to be expressed differentially compared with WT mice, comprising 57 downregulated proteins and 30 upregulated proteins (Fig. 6A).

Twenty-six sperm fibrous sheath-associated proteins and 26 mitochondrial sheath-associated proteins have been summarized by previous research (Lehti and Sironen, 2017). Among these, 22

Table 2. Semen analyses for WT, OE and KI male mice by CASA

Parameter	WT*	KI*	OE [†]	<i>P</i> -value ^{KI versus WT}	<i>P</i> -value ^{OE versus WT}
Concentration (mill/ml)	27.79±6.23	13.3±2.85a	30.24±5.76	0.007	0.46
Viability (%)	96.24±1.93	86.50±3.04a	93.52±2.17	0.0005	0.03
Motility [§]					
A-level motility (%)	5.77±1.25	3.61±0.48	5.55±1.04	0.025	0.68
B-level motility (%)	71.67±8.29	41.86±1.25 a	62.14±7.19	0.0005	0.04
C-level motility (%)	18.80±6.01	41.08±2.34 a	25.84±5.37	0.0005	0.04
D-level motility (%)	3.76±1.93	13.45±3.04 a	6.48±2.17	0.0006	0.03
VCL (µm/s)	72.34±8.08	51.40±6.87 a	61.98±7.25	0.0066	0.03
VSL (µm/s)	14.75±1.37	9.11±1.02 a	13.26±1.01	0.0004	0.04
VAP (µm/s)	31.47±2.98	21.79±2.97 a	27.50±2.45	0.002	0.02
LIN (%)	20.52±2.28	17.77±0.50	21.53±1.90	0.08	0.38
STR (%)	46.96±3.24	41.93±1.67	48.31±2.54	0.04	0.40
WOB (%)	43.60±1.93	42.38±0.50	37.90±1.40	0.33	0.37

LIN, linearity; mill/ml, million per ml; STR, straightness; VAP, average path velocity; VCL, curvilinear velocity; VSL, straight-line velocity; WOB, wobbling.

**n*=6, age of ~20 weeks.

[†]*n*=8, age of ~20 weeks.

[§]Motility levels: A-level motility, sperm move forward rapidly; B-level motility, sperm move forward slowly; C-level motility, sperm move in a nonforward direction; D-level motility, sperm move extremely slowly or remain static.

fibrous sheath-associated proteins (Akap4, Akap3, Gapdhs, Ldhc, Spa17, Fsp1, Fsp2, Ropn1, Ropn11, Ldha, Pde4a, Tekt2, Fscb, Cabyr, Hk1, Aldoa, Slc25a31, Gapdh, Rhpn2, Gsk3b, Stat1 and Gstm5) and 15 mitochondrial sheath-associated proteins (Klc3, Spata19, Tekt5, Prkar2a, Srsf10, Selenop, Cfap157, Vdac2, Ppp1cc, Gpx4, Tssk2, Ak2, Tex22, Nectin2 and Gopc) were detected in both the KI and OE proteomic data. Gene Set Enrichment Analysis (GSEA) showed that the 22 proteins associated with the fibrous sheath were significantly enriched in the downregulated proteins of KI mice and the upregulated proteins of OE mice (Fig. 6B; *q*<0.05). In addition, the 15 mitochondrial sheath-associated proteins and the 73 acrosomal vesicle-associated proteins showed a similar trend (Fig. 6B), despite being nonsignificant in OE mice (*q*>0.05).

Twelve fibrous sheath-associated proteins, nine mitochondrial sheath-associated proteins and 32 acrosomal vesicle-associated proteins, which were downregulated in KI mice and upregulated in OE mice simultaneously when compared with WT mice, accounted for 46.2% (12/26), 34.6% (9/26) and 43.8% (32/73) of known fibrous sheath-, mitochondrial sheath- and acrosomal vesicle-associated proteins, respectively (Fig. 6C). To validate the conclusions of our proteomics analysis, we performed western blotting and sperm immunostaining on Akap4, Akap3, Cabyr, Gapdhs and Odf2. The results indicated upregulation and downregulation of Akap4, Akap3, Cabyr and Gapdhs in the testes of OE and KI mice, respectively (Fig. 6D). This trend was not typical of Odf2, for which we observed decreased expression in KI mice but no increased expression in OE mice. Furthermore, staining of Akap4, Akap3 and Cabyr was absent in KI sperm, whereas Gapdhs and Odf2 staining depicted shorter and disorganized sperm tails in KI sperm (Fig. 6E).

Two feature motifs of Fsp2 are identified in species with internal fertilization

To reveal the sequence characteristics of Fsp2, we investigated the functional domains of human FSIP2 with a protein-domain prediction tool. Three FSIP2 domains were recognized (Fig. 7A), whereas the functions of the other regions of FSIP2 remained unelucidated. In light of this, we explored conserved motifs of Fsp2 using the Multiple EM for Motif Elicitation (MEME) online tool. Eight species (*Homo sapiens*, *Mus musculus*, *Pogona vitticeps*, *Latimeria chalumnae*, *Acanthaster planci*, *Bombyx mandarina*,

Mizuhopecten yessoensis and *Stylophora pistillata*) were enrolled. A total of 30 motifs were identified in the eight species (Fig. 7B), 29 of which were included in *H. sapiens* and *M. musculus* (except for the 7th motif). Fsp2 of *S. pistillata*, *M. yessoensis*, *B. mandarina*, *A. planci*, *L. chalumnae* and *P. vitticeps*, consisted of two, four, three, six, seven and 21 motifs, respectively, showing an increasing tendency commensurate with organismal evolution.

In *H. sapiens*, *M. musculus* and *P. vitticeps*, tandem repetition of the first and third motifs was observed in the proximal C-terminal regions (Fig. 7B), corresponding to the three FSIP2 domains (Fig. 7A). Notably, the nonrepetitive sixth and fifth motifs [the 6518-6648 amino acid (aa)-segment in the human FSIP2 protein, Fig. 7C], which did not appear in *A. planci*, *B. mandarina*, *M. yessoensis* or *S. pistillata*, were only found in the C-terminal region of more complex life forms. *H. sapiens*, *M. musculus*, *P. vitticeps* and *L. chalumnae* show internal fertilization, whereas *A. planci*, *B. mandarina*, *M. yessoensis* and *S. pistillata* have external fertilization. This observation suggested that the sixth and fifth motifs in the C-terminal region are associated with internal fertilization.

DISCUSSION

FSIP2 is one of the largest proteins in humans, and its mutations can cause MMAF phenotypes (Martinez et al., 2018; Liu et al., 2019a). In this work, we detected a homozygous truncating mutation of FSIP2 in a patient with MMAF, which prompted us to investigate the underlying molecular mechanism by establishing mouse models for Fsp2. The Fsp2-KI mouse model mimicked the mutation and, as expected, exhibited MMAF phenotypes typical of those observed in the sperm of the patient. Additionally, reduced mRNA expression levels of Fsp2 were detected in KI mice, in agreement with a previous observation suggesting nonsense-mediated mRNA decay of FSIP2 (Liu et al., 2019a). By contrast, longer principal pieces and MPs were observed in the sperm of the Fsp2-OE mouse model, manifesting as the aforementioned 'super-long' sperm. To the best of our knowledge, this is the first report of a transgenic mouse model with elongated sperm. The reciprocal morphology of sperm from KI and OE mice provides preliminary evidence of this vital role of Fsp2 in the development of the sperm flagellum.

The transcriptome profiles of mouse testes were revealed recently, which provided a high-resolution cellular atlas, discriminative cell markers and previously unknown stage regulators of male germ cell development (Green et al., 2018; Chen et al., 2018; Lukassen et al., 2018; Jung et al., 2019). In the present study, we used single-cell

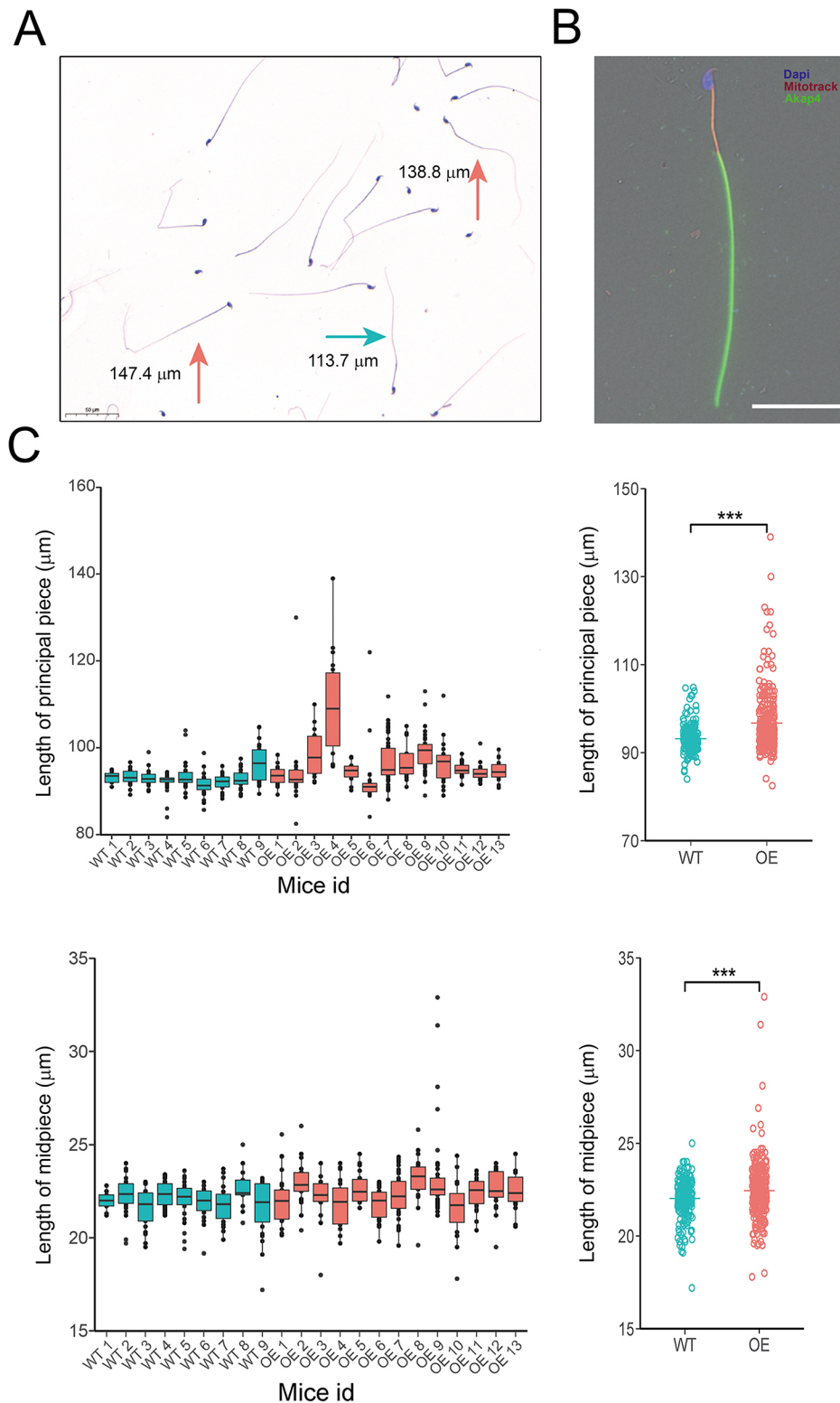


Fig. 3. Overexpression of *Fsip2* leads to elongation of sperm principal piece and MP. (A) Diff-Quick staining reveals some longer spermatozoa observed in OE mice. Red and blue arrows indicate the super-long and normal-length sperm, respectively. (B) Schematic showing the length measurement for the principal piece and MP of a sample sperm. (C) Box plots indicating the lengths of principal pieces and MPs of WT ($n=11$) and OE ($n=7$) mice sperm, and bubble plots representing the group-wise comparisons of principal piece and MP lengths. The box represents the median (horizontal line inside the box), 25% and 75% interquartile (lower and upper horizontal lines of the box); the whiskers show the minimum and maximum. The outliers are indicated by the points outside of the box-and-whiskers. The boxes are colored according to the genotypes. Bubble plot data are mean \pm s.d. P -values were calculated using the two-tailed t -test. *** $P<0.001$. Scale bars: 25 μ m in B; 50 μ m in A.

RNA-seq to explore the alterations in gene expression profiles induced by the mutation and overexpression of *Fsip2*. The results showed that *Fsip2* was widely expressed in all six cell types, with highest expression in round spermatids, in accordance with a previous study that suggested *Fsip2* as a marker of round spermatids (Green et al., 2018). Interestingly, the genes upregulated among the four subclusters of round spermatids of OE and WT mice were involved in sperm flagellum development, consistent with the elongated tails

observed in OE-mouse sperm. In addition, the upregulated genes were also significantly enriched in the GO terms concerning spermatid development. This result agreed with our *Odf2* immunofluorescence observations of the advanced development of spermatids at stage XI-XII in the seminiferous tubules of OE mice relative to WT and KI mice (Fig. S2), suggesting that overexpression of *Fsip2* leads to an acceleration of spermatid development. By contrast, far fewer differentially expressed genes were found among

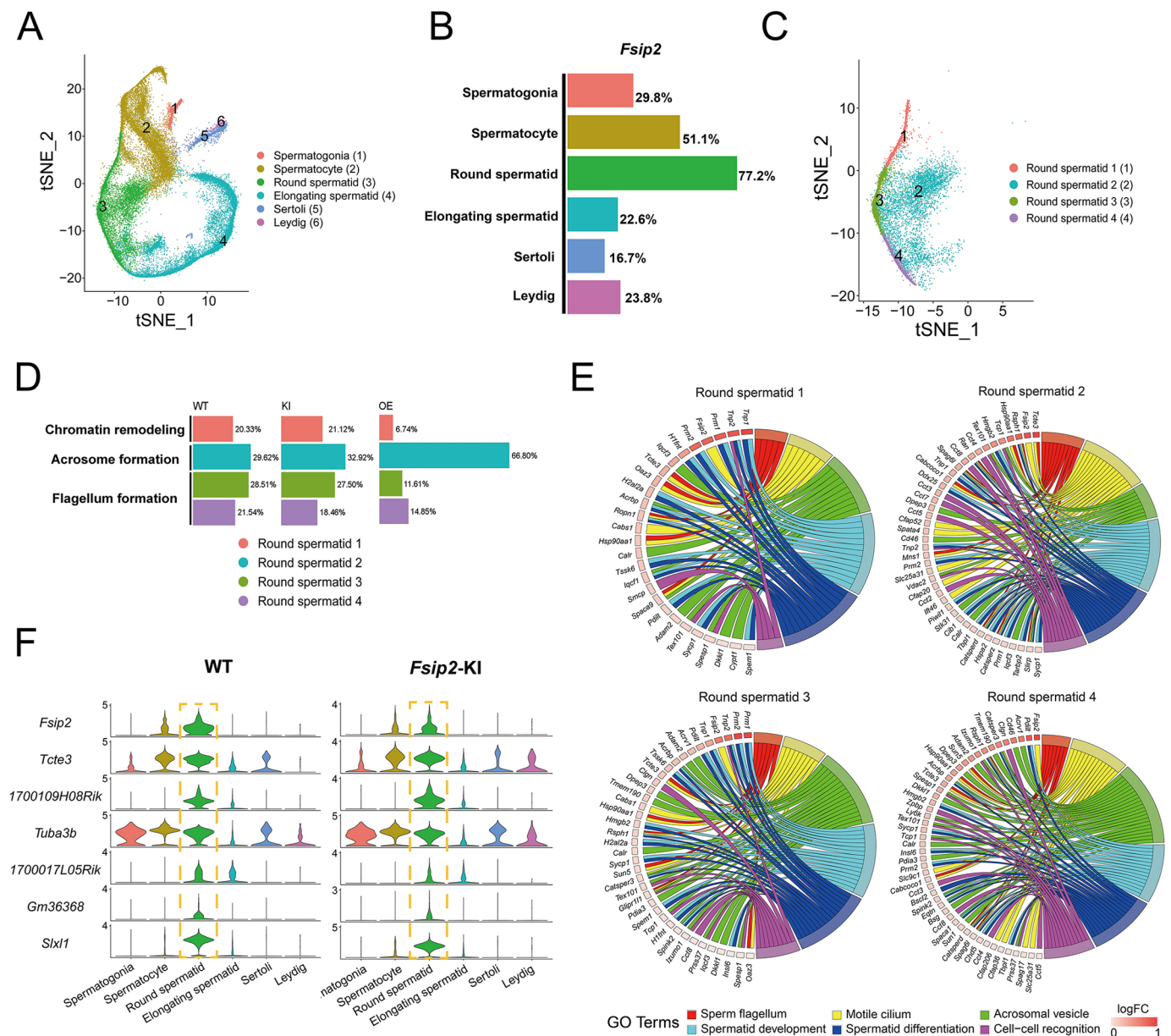


Fig. 4. Alteration of testis gene expression profiles induced by overexpression and mutation of *Fsp2*. (A) t-Distributed stochastic neighbor embedding (tSNE) plot displaying 39,502 cells from WT, OE and KI mice separated into six testis cell types; $n=3$. (B) The percentage of cells expressing *Fsp2* in six cell types of WT, KI and OE mice; $n=3$. (C) tSNE plot displaying four subclusters of round spermatids. (D) Cell proportions of round spermatids 1-4 of WT, KI and OE mice, affiliated with functional relevance. (E) GO enrichments of genes upregulated among the four subclusters of round spermatids of OE and WT mice. (F) Stacked violin plots exhibiting the expression profiles of the top downregulated genes between KI and WT mice. Their expression in the round spermatid clusters of WT and KI mice is highlighted by orange boxes.

the round spermatids 1-4 of KI and WT mice, indicating that the mutation in *Fsp2* exhibited a minor influence on the testicular expression profile. One of the top downregulated genes, *Tcte3*, is reported to encode a dynein light chain and disruption of *Tcte3* in a mouse model resulted in asthenozoospermia (Rashid et al., 2010).

The proteomes of testes or sperm from *Qrich2*-, *Akap4*- and *Akap3*-deficient mice have been explored, from which the molecular basis of MMAF was determined (Shen et al., 2019; Fang et al., 2019; Xu et al., 2020). Herein, we also used a proteomics approach to reveal the impact of truncation and overexpression of *Fsp2* on testis protein expression. GSEA analysis indicated that the 22 proteins associated with the fibrous sheath and 15 proteins associated with the mitochondrial sheath were simultaneously

enriched in the downregulated proteins of KI mice and the upregulated proteins of OE mice. The 11 proteins associated with ODF also showed a similar tendency, although the enrichments were not significant (Fig. S3; $q>0.05$). According to the literature, five of these proteins (*Akap4*, *Akap3*, *Cabyr*, *Gapdhs* and *Odf2*) are associated with the sperm tail, and their complete disruption significantly impairs the development of sperm flagella or sperm motility in mouse models (Xu et al., 2020; Miki et al., 2002, 2004; Donkor et al., 2004; Young et al., 2016). Our western blot analysis confirmed the upregulation and downregulation of *Akap4*, *Akap3*, *Cabyr* and *Gapdhs* in the testes of OE and KI mice, whereas *Odf2* did not exhibit significantly increased expression in OE mice.

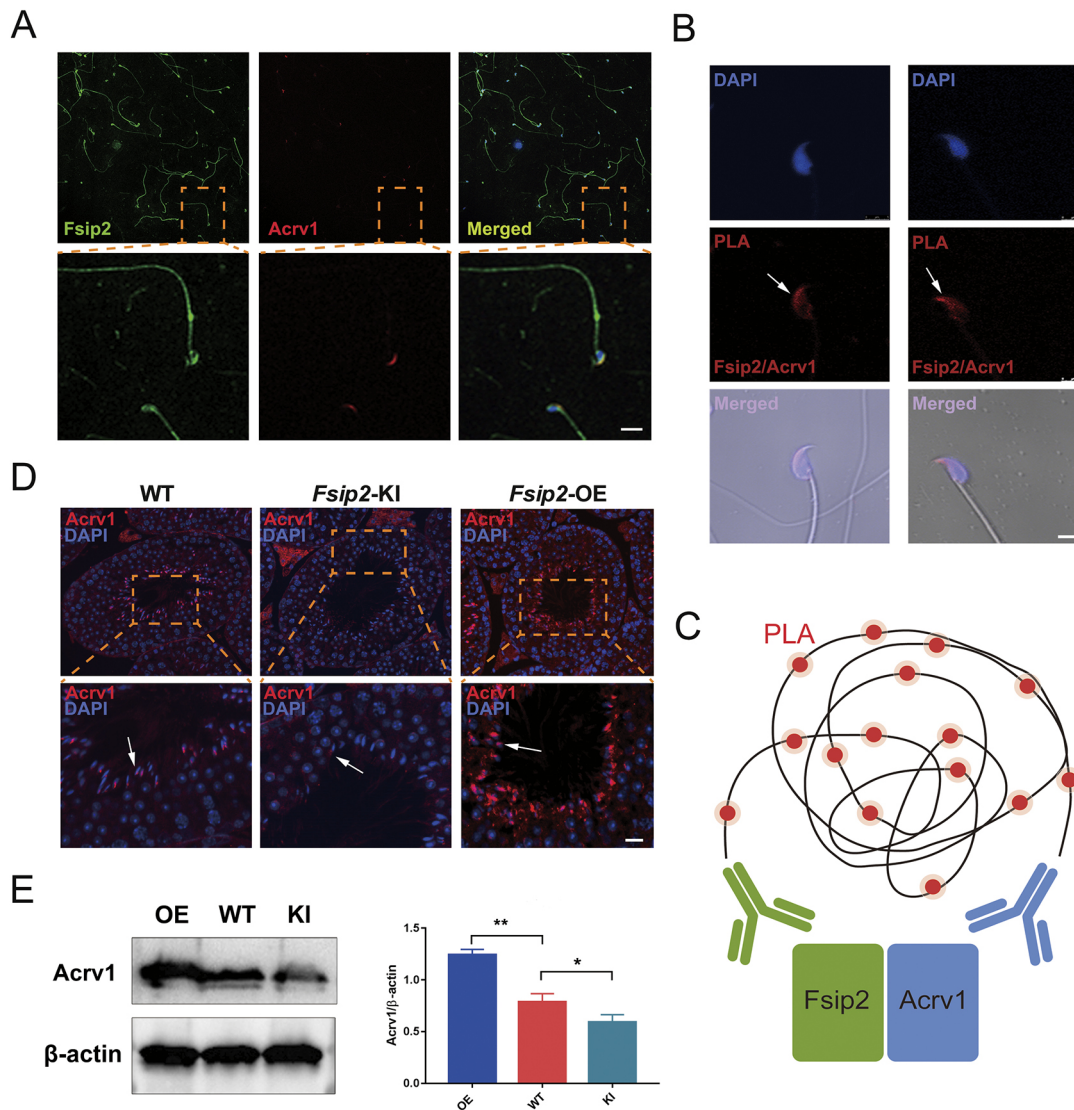


Fig. 5. Fsp2 interacts with acrosomal protein Acrv1. (A) Immunofluorescence staining of cauda spermatozoa of WT mice showing the co-expression of Fsp2 (green) and Acrv1 (red). The dashed orange lines indicate the magnified area below. (B) Duolink *in situ* assessment reveals the physical interaction between Fsp2 and Acrv1 in WT sperm. The left and right panels each represent two WT sperm. The nuclear marker DAPI (blue; top), PLA signal (red; middle) and the merged view (bottom) are shown. (C) Schematic representing *in-situ* Proximity Ligation Assay (PLA) for Fsp2-Acrv1 interaction. (D) Immunostaining of Acrv1 (red) in seminiferous tubules of testicular sections at stage VII-VIII. Top images show tissue immunostaining of WT, *Fsp2*-KI and *Fsp2*-OE mice; bottom images show the corresponding magnified views. The white arrows indicate Acrv1 staining. The nuclear marker DAPI is in blue. The dashed boxes indicate the magnified area. (E) Western blot analysis of Acrv1 protein expression in mouse testis, with β -actin used as the internal control. The graph shows the statistical differences for three independent experiments. $n=3$. Data are mean \pm s.d. *P*-values were calculated using the two-tailed *t*-test. **P*<0.05. Scale bars: 5 μ m in B; 10 μ m in A,D (magnified views); 25 μ m in D.

Previous findings using sperm immunofluorescence staining corroborate the absence of FSIP2 in the principal piece of sperm from a patient with MMAF (Liu et al., 2019a). Herein, also using immunofluorescence staining, we showed that Fsp2 was expressed in the principal piece, MP and sperm head. Duolink PLA further confirmed the interaction between Fsp2 and Acrv1 in the acrosome. Additionally, expression of Acrv1 was significantly increased and decreased in OE and KI mice, respectively. These results, together with the findings that upregulated genes of round spermatids in OE mice were enriched in the acrosomal vesicle and that the acrosomal vesicle-associated proteins were reciprocally affected by the dosage alterations of Fsp2, collectively suggest a fascinating role of Fsp2 in the acrosome.

A full understanding of the sequence characteristics of human FSIP2 has proved elusive. The use of a conventional protein domain

prediction tool was unable to provide sufficient information because only three of the FSIP2 domains were recognized (Martinez et al., 2018). Here, using a motif discovery tool, we observed conserved motifs of Fsp2 in eight species. Intriguingly, among the identified motifs, the sixth and fifth motifs were only conserved in the species with internal fertilization, suggesting a potential connection between these two motifs and internal fertilization. Coincidentally, a recent study found that the accessory structure (fibrous sheath) of the flagellum enhanced the progressive motion of mammalian sperm in high-viscosity media (Gadêlha and Gaffney, 2019), representative of the internal fertilization environment. Conversely, the migration of sea urchin sperm lacking a fibrous sheath was significantly compromised in the same environment (Gadêlha and Gaffney, 2019). These results indicated that the fibrous sheath is essential for internal fertilization. In

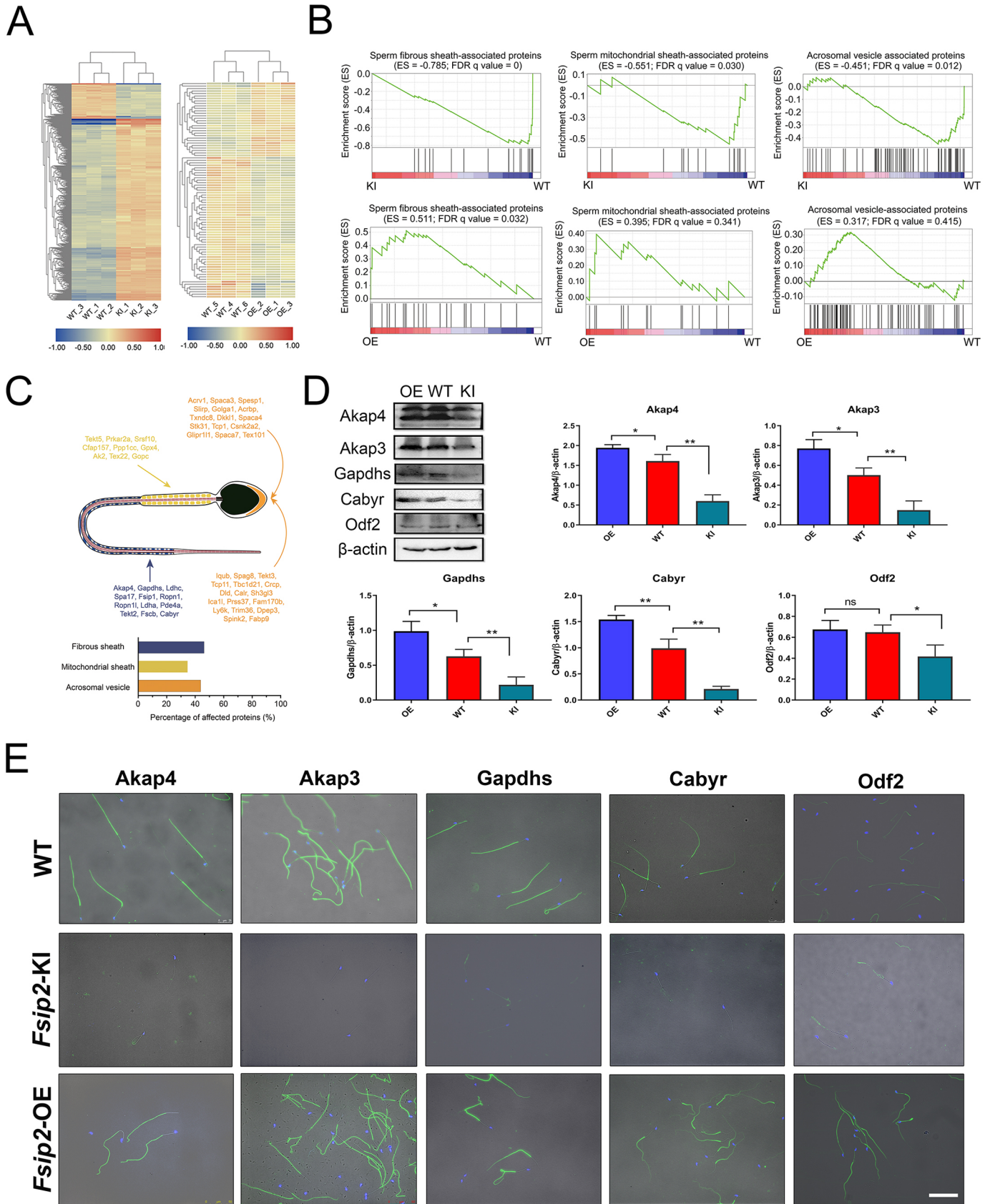


Fig. 6. See next page for legend.

Fig. 6. Proteins involved in fibrous sheath, mitochondrial sheath and acrosomal vesicle formation are downregulated in KI mice and upregulated in OE mice. (A) Heat maps from three independent proteomic analyses of testis samples from WT, KI, and OE mice. $n=3$. (B) GSEA showing the enriched proteins associated with the fibrous sheath, mitochondrial sheath and acrosomal vesicle that are downregulated in KI mice and upregulated in OE mice. (C) Schematic of the structure of a spermatozoan. Proteins that were downregulated in KI mice and upregulated in OE mice are shown in blue (fibrous sheath), yellow (mitochondrial sheath) and orange (acrosomal vesicle). The percentages of these proteins are also indicated in the bar plot. (D) Western blot analyses of testicular tissues for the sperm tail proteins Akap4, Akap3, Gapdhs, Cabyr and Odf2. β -actin was used as the internal control. $n=3$. Data are mean \pm s.d. P -values were calculated using the two-tailed t -test. * $P<0.05$, ** $P<0.01$. ns, not significant. (E) Immunofluorescence staining of Akap4, Akap3, Gapdhs, Cabyr and Odf2 on WT (top), KI (middle) and OE (bottom) spermatozoa. Scale bar: 20 μ m in E.

addition, a patient with MMAF with a 5463-aa truncation in FSIP2 exhibited an MMAF phenotype similar to those of three other patients in whom FSIP2 was truncated to sequences as short as 304 aa, 536 aa and 761 aa (Martinez et al., 2018). This implies that the region of FSIP2 required for fibrous sheath formation is beyond 5463 aa and located in the C-terminal region. Given that fibrous sheaths are unique to sperm of internally fertilized species, it could be inferred that the C-terminal region is indispensable for internal fertilization, in accordance with our conclusions drawn from our motif analysis.

Interactions among Cabyr, Ropn1 and Akap3, and between Akap3 and Akap4 have been validated (Brown et al., 2003; Li et al., 2011). *Fsip2* was also found to bind Akap4, probably with the 1040-1705-aa segment (Brown et al., 2003). However, three patients in whom FSIP2 was longer than 2500 aa still presented with typical MMAF phenotypes (Martinez et al., 2018; Liu et al., 2019a). In addition, AKAP4 immunostaining was absent in sperm that carried a truncated FSIP2 of 5463 aa from the patient with MMAF (Martinez et al., 2018). Therefore, we speculate that there are two binding sites for AKAP4 on FSIP2, the first located in the 1040-1705-aa segment and the second residing on the C-terminal region, i.e., the sixth and fifth motifs, respectively, with the second binding site being indispensable for the formation of the fibrous sheath.

We hereby propose a molecular mechanism for MMAF induced by FSIP2 truncated mutations. Under physiological conditions, ROPN1 and CABYR bind AKAP3, which also interacts with AKAP4. AKAP4 binds the two binding sites of FSIP2 simultaneously to form the normal fibrous sheath and sperm flagellum. However, when FSIP2 is truncated because of loss-of-function mutations, the second binding site is lost, which significantly impairs the interaction with AKAP4, leading to the MMAF phenotypes.

In summary, our experiments and analyses based on mouse models with hypermorphic and hypomorphic alleles indicated dual crucial roles for *Fsip2* in sperm tail and acrosome formation. The molecular mechanism underlying the MMAF phenotypes caused by mutations in *FSIP2* was also elucidated. Our findings, together with previously reported recurring amplifications of *FSIP2* in testicular germ cell tumors (Litchfield et al., 2015), suggest a complex role for *Fsip2* in sperm-egg recognition, spermatogenesis and tumorigenesis.

MATERIALS AND METHODS

Patient with MMAF

An infertile 28-year-old man, found to have asthenozoospermia at the Center of Reproductive Medicine, Guangzhou Women and Children's Medical Center, was enrolled in this study. Semen samples were collected by masturbation after 2-7 days of sexual abstinence and were examined after liquefaction for 30 min

at 37°C. The analysis was repeated three times over 3 months. The study was approved by the ethics committee of Guangzhou Women and Children's Medical Center. Informed consent was obtained from the patient.

Whole-exome sequencing and Sanger sequencing

Genomic DNA (gDNA) was extracted from the peripheral blood of the patient. WES and data analysis were performed as described previously (Sun et al., 2019). The insertion mutation found by WES was further confirmed by PCR using Q5 High-Fidelity Polymerase (5 \times , NEB), with the specific primers targeting the selected candidate variant (forward: 5'-AAG-GTGAGCCCTAAGGACAA-3'; reverse: 5'-TTTGGCTTACCCGATGA-AAT-3'). The PCR products were then validated by Sanger Sequencing.

Generation of the *Fsip2*-knock-in mouse model

The animal experiments were approved by the Experimental Animal Ethics Committee of Guangzhou Medical University; all animal experiments were performed in accordance with the guidelines and regulations of the Committee. To mimic the *FSIP2* mutation (c.8368_8369insC, p.2790fs) found in the patient with MMAF, an *Fsip2*-KI mouse line (c.8137insC) was generated by homology-dependent DNA repair using the genome-editing method based on CRISPR-Cas9 technology. All mice used in this study were of a C57BL/6J genetic background. Guide RNA used was 5'-ATC-AAGAACAAGTTATCTGCTGG-3' and donor DNA was 5'-AGCAG-TACTAAGACCCAAAATCAAGAACAAGTTAagcGCTGGAGAGAAA-AcCTCCAAGAGAGAGCAGACCAAAAACCGCCCTTGGGCTGCCAC-AACTCCAC-3'. The mixture of Cas9 mRNA, gRNA and donor DNA was injected into fertilized eggs with recognized pronuclei from superovulated 6- to 8-week-old female C57BL/6J mice in M2 medium. The injected zygotes were cultured in an environmentally controlled incubator with 5% CO₂ at 37°C, and the blastocysts obtained were then transferred into the uteri of pseudo-pregnant C57BL/6J females. The inserted mutation was confirmed using PCR on the offspring. The genotyping primers used were as follows: forward, 5'-AACTCAGCCCA-AAGAACAGCCC-3'; reverse, 5'-TCCGTAGGATAACCTGCACCCA-3'.

Generation of the *Fsip2*-overexpression mouse model

Transgenic mice in a C57BL/6J background were generated by using BAC clone ID RP23-221K3 (CloneDB, <https://www.ncbi.nlm.nih.gov/clone/669242/>), which included *Fsip2* and its flanking sequences. The BAC DNA (1 ng/ μ l in circular form) was injected into fertilized oocytes and integrated into the genome randomly. The integration of the BAC clone into the mouse genome was confirmed using PCR primers at each end of the BAC sequence: 5' reaction, 290 bp (forward: 5'-CAGCAAGGAAACAA-TGGTTACAC-3'; reverse: 5'-CCAGAAGTGCAGTCGTAAAAGTC-3'); 3' reaction, 545 bp (forward: 5'-TCCGCACCCGACATAGATAATAAC-3'; reverse: 5'-CATGACTGCTCTGACAACACAC-3'). The copy number of *Fsip2* was determined as previously described (Habib et al., 2018). First, the mouse genomic DNA was extracted using DNeasy Blood and Tissue Kit (Qiagen), according to the manufacturer's instructions. Second, to estimate the copy number of *Fsip2*, the qPCR reaction mixture was prepared by adding 10 ng of the genomic DNA into PowerUp SYBR Green Master Mix (A25742, Applied Biosystems) containing 10 mM of the following primers: *Fsip2* 247 bp (forward: 5'-AAATGAGCAAAAAGCCAGGGG-3'; reverse: 5'-CTGTTCCGGGTGTTTTCTGCA-3') and *Dicer1*, 260 bp (forward: 5'-CTGGTGGCTTGAGGACAAGAC-3'; reverse: 5'-AGTGTAGCCTT-AGCCATTTGC-3'). The reaction mixture was subjected to real-time qPCR for 40 cycles on the Applied Biosystems System Quant 6 flex.

The $\Delta\Delta$ CT method was used for data analysis. Each assay was performed in triplicate for each sample. *Dicer1* was used as the copy number reference (two genomic copies). The copy number for *Dicer1* was constant in both WT and OE mice (Habib et al., 2018). The copy number of *Fsip2* was two for the WT littermates.

Real-time qPCR

Total RNA was extracted from the testes using TRIzol kit (15596026, Life Technologies), followed by RNA purification using Direct-zol RNA mini prep (R2050, Zymo Research). cDNA was synthesized using the

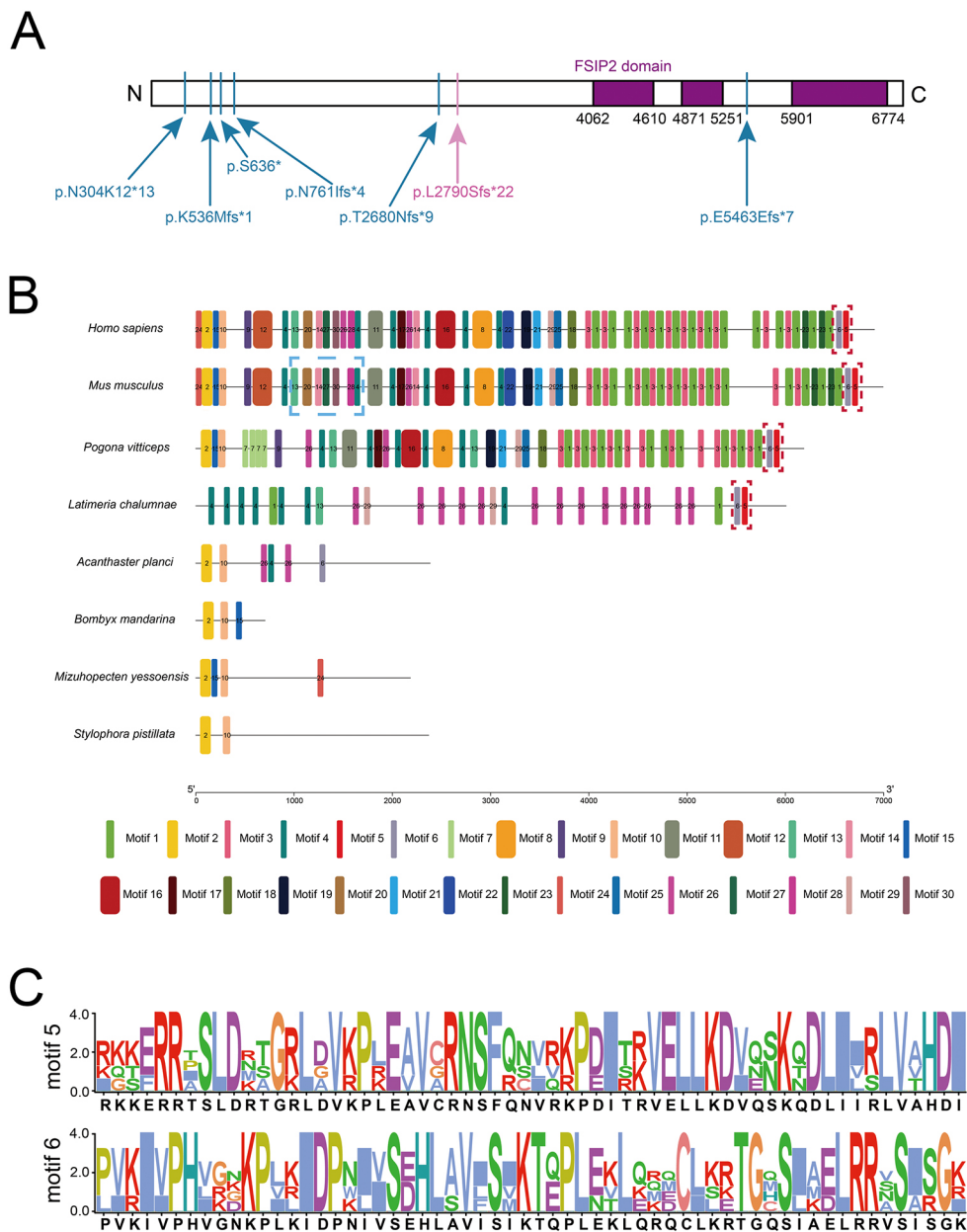


Fig. 7. Sequence characteristics of Fsp2. (A) Locations of disease-related mutations in the human FSIP2 protein. Mutations reported previously (Martinez et al., 2018; Liu et al., 2019a) and found in this study are indicated in blue and pink, respectively. Three FSIP2 domains predicted by the SMART server (<http://smart.embl-heidelberg.de/>) are shown as purple boxes. (B) Motifs identified in FSIP2 of *Homo sapiens* and seven other species (*Mus musculus*, *Pogona vitticeps*, *Latimeria chalumnae*, *Acanthaster planci*, *Bombyx mandarina*, *Mizuhopecten yessoensis* and *Stylophora pistillata*) using the MEME tool (<http://meme-suite.org/tools/meme>). The binding site of Akap4 on Fsp2 (1040-1705 aa) as proposed by Brown et al. (2003), and the C-terminal fifth and sixth motifs, are outlined by blue-dashed and red-dashed boxes, respectively. (C) Sequence composition of the fifth and sixth motifs of FSIP2.

Thermoscript RT-PCR system (1713181, Invitrogen). Real-time qPCR reactions were carried out using two sets of primers, one close to the 5' end of *Fsp2* (forward: 5'-TCACACGATTCCAAAAGTGG-3'; reverse: 5'-AAGCGTTGTTCTCTGCTGT-3'), and the second close to the 3' end of *Fsp2* (forward: 5'-TGATGAGGAGGAGGTTGTCC-3'; reverse: 5'-TTTCAGGTTGCTTGCTTG-3'). *Gapdh* served as the reference (forward: 5'-ATCCAGAATACATGGTTTAC-3'; reverse: 5'-GTTGATCTCAAGGTTGTC-3').

Fertility assessment

The fertility of each genotype was tested using adult male mice (8-12 weeks old). Briefly, a male mouse was caged with two WT female mice. Vaginal plugs were checked for each morning; once a vaginal plug was identified (day 1 post coitus), the female with the vaginal plug was placed in a separate cage and the male was allowed to rest for 2 days. Another female was then placed in the cage for another round of mating. The female was deemed not pregnant if it had not generated any pups by day 22 post coitus, and it was euthanized to confirm the lack of pregnancy. At least 20 mice were tested for each gender and genotype.

Sperm viability, motility and morphology assessments

Cauda epididymal sperm were collected immediately from adult male mice after euthanization and washed with PBS. The sperm were then released by making an incision in the epididymal tissue, placed in Sperm Rinse medium (Vitrolife) and allowed to swim up for 30 min at 37°C. Sperm viability and motility was examined using the Automatic Sperm Cytomorphology Analyzer (CASA) system with phase-contrast microscopy (Microptic S.L.). For morphology assessments, Papanicolaou (BASO) staining of mouse sperm was performed. Briefly, the smears prepared from the epididymal cauda sperms isolated above were fixed in 95% ethanol for 15 min, rehydrated in an ethanol gradient and stained with Papanicolaou staining according to the manufacturer's instructions (DA0191, Leagene Biotechnology).

Scanning and transmission electron microscopy

For SEM, spermatozoa samples were isolated, washed in PBS and fixed in 2.5% glutaraldehyde and 2% paraformaldehyde in 0.15 M sodium phosphate buffer overnight at 4°C. The sperm were then washed in the buffer and collected on Nucleopore filters or glass coverslips, subjected

to critical point drying and coated with gold/palladium. Samples were examined in a HITACHI S-3000N scanning electron microscope at 20 kV.

For TEM, spermatozoa samples were fixed under the same conditions as described for SEM, postfixed in 2% osmium tetroxide in cacodylate buffer and embedded in Lowicryl resin. Sections were stained with uranyl acetate and lead citrate, and examined in a Hitachi H-7500 transmission electron microscope at 80 kV.

Sperm immunostaining

The cauda epididymis sperm were isolated as described above, fixed with 4% paraformaldehyde (PFA) or 95% ethanol, permeabilized with freshly prepared 0.3% Triton X-100 in PBS, blocked with 10% goat serum for 1 h at 37°C and then incubated with primary antibodies (Table S3) with optimal dilution overnight at 4°C. The slides were allowed to stand at room temperature (RT) for 1 h and were then washed and incubated with secondary antibody Alexa Fluor 488 goat anti-rabbit IgG (H+L) (Table S1) for 1 h at RT. Finally, the slides were washed and mounted using anti-fade mounting media with DAPI. The images were captured at high magnification using a fluorescence microscope with a phase-contrast channel (Leica Microsystems).

Assessment of length of MPs and principal pieces of sperm

To estimate the length of MPs and principal pieces of sperm of OE and WT mice, we used the immunostaining method described above in combination with phase-contrast microscopy. The MP and principal piece were stained with MitoTrack (red) and Akap4 antibody (green), respectively. The measurements were performed using Leica microscopy image processing and quantification tools. At least 100 sperm from each sample were used to estimate the length of the MP and principal piece.

Processing and morphology assessment of testes

Testes were surgically removed and fixed in modified Davidson's Fluid (mDF) (ServiceBio), dehydrated in ascending grades of ethanol and embedded in paraffin. Then, 3- to 4- μ m-thick sections were prepared. For the histological assessments, sections were stained with Hematoxylin and Eosin according to the standard protocol. PAS staining was also conducted on sections from the testis using periodic acid solution and Schiff's reagents (395B, Sigma-Aldrich). The morphology was observed and captured using PANNORAMIC slide scanners (3DHITTECH); the images were processed and exported using CaseViewer (version 2.4).

Tissue immunostaining

Paraffinized fixed testicular tissue sections were hydrated in descending grades of ethanol, followed by antigen heat activation using citrate buffer (pH 6) for 20 min. The slides were then permeabilized with 0.3% Triton X-100, blocked with 10% goat serum for 1 h at RT and incubated with primary antibodies (Table S3) overnight at 4°C. Next, the slides were allowed to stand for 1 h at RT, followed by two washes with PBS for 5 min, incubated with the secondary antibody (goat anti-rabbit Alexa Fluor 488 or goat anti-mouse Alexa Fluor 568; A11034 or A11004, Invitrogen; Table S3) and mounted with Fluoroshield with DAPI (ab104139, Abcam). Images were acquired using a fluorescence microscope (Leica).

Western blotting

The total protein was extracted from the mice testes. Approximately 50 mg of testes were homogenized on ice with prechilled RIPA lysis buffer containing a 10 mM cocktail protease inhibitor (Roche) and PMSF using a tissue homogenizer, allowed to set for 30 min with occasional shaking, centrifuged at 12,000 RPM (16,000 g) for 15 min, followed by denaturation at 95°C for 10 min with 4 \times loading buffer (Bio-Rad) containing 2-mercaptoethanol (Sigma-Aldrich). The denatured proteins were separated on SDS-polyacrylamide gels and transferred to a PVDF membrane for immunoblotting analyses. β -actin was used as the loading control.

Duolink Proximity Ligation Assay

The protein-protein interaction between Fsp2 and Acrv1 was detected using the Duolink PLA kit (Duolink In Situ Red Starter Kit Mouse/Rabbit, DUO92101, Sigma-Aldrich). The protein-protein interaction was indicated when a red signal with DuoLink PLA was generated (i.e. when the physical distance between the two proteins was less than 20 nm). According to the manufacturer's instructions, the sperm smear slides were fixed and permeabilized, blocked with Duolink Blocking Solution at 37°C in a preheated humidity chamber for 60 min and then incubated overnight at 4°C with antibodies raised from two different species [i.e. rabbit anti-Fsp2 antibody (bs-16187R, Bioss) and mouse anti-Acrv1 antibody (sc-398536, Santa Cruz Biotechnologies)]. Next, the smears were washed and incubated with Duolink PLA Probe PLUS and MINUS diluted in antibody diluent buffer for 1 h at 37°C. Unbound PLA probes were removed with washing buffer A, followed by ligation steps for 30 min at 37°C. The PLA signal was amplified by incubating the slides with amplification solution for 100 min at 37°C. Finally, the slides were washed with buffer B, mounted using Duolink In Situ Mounting Medium with DAPI and captured using a confocal microscope (Leica TCS SP8 Microsystems).

RNA-seq library preparation for 10x Genomics single-cell sequencing

Testes of WT, KI and OE mice were isolated and dissociated into single-cell suspensions as previously described (La Salle et al., 2009). Three mice were used for each genotype. Briefly, the testis was excised and the tunica albuginea was removed. Seminiferous tubules were digested with Collagenase IV (C5138, Sigma-Aldrich), trypsin from bovine pancreas (T9201, Sigma-Aldrich) and DNase I from bovine pancreas (14365, USB), lyophilized, filtered and resuspended. For each sample and prepared libraries, ~5000 cells were loaded into one channel of the Chromium system according to the protocol of 10x Genomics. The sequencing process was conducted on an Illumina HiSeqX machine in a paired-end 150 bp mode.

Preprocessing of single-cell RNA-seq data

The Cell Ranger v3.0.0 mkfastq (10x Genomics) was used to demultiplex the cellular barcodes. Adapters, low-quality reads and low-quality bases were removed using Trimmomatic software (Bolger et al., 2014). Basic statistics of the quality of the clean data reads was performed with FastQC.

The clean reads were aligned to the murine reference genome (mm10) using the Cellranger count command. The R package Seurat (3.1.0) (Satija et al., 2015) was applied to convert the unique molecular identifier (UMI) count matrix to Seurat objects. The genes expressed in fewer than ten cells and cells with fewer than 200 expressed genes were removed. The expression data were normalized using the NormalizeData function, in which the UMI counts were divided by the total number of UMIs per cell, multiplied by 10,000 for normalization and then log-transformed. After normalization, 2000 highly variable genes were identified using the FindVariableGenes function. We then used the FindIntegrationAnchors and IntegrateData functions to combine the nine samples from WT, KI and OE mice. Principal component analysis (PCA) was performed with the RunPCA function. The top 30 PCA components were used for the RunTSNE function and the FindClusters function. Fourteen clusters were identified for WT, KI and OE mice. The marker genes were found using the FindConservedMarkers function.

Identification of major cell types and subclusters

Marker genes for major cell types in the murine seminiferous tubule have been proposed previously (Green et al., 2018), which were used to identify the major cell types of clusters 1-14. The eighth, fifth, second and fourth clusters were recognized as elongating spermatids. The tenth, sixth, third and eleventh clusters were recognized as round spermatids. The ninth, twelfth and first clusters, and the seventh cluster, were recognized as spermatocyte and Sertoli cells, respectively. The thirteenth and fourteenth clusters were recognized as spermatogonia and Leydig cells, respectively. Twelve subclusters of WT, KI and OE mice that were recognized as round spermatids were extracted and analyzed. The differential expressed genes

between the corresponding subclusters of OE and WT mice and between KI and WT mice were analyzed with the function FindMarkers. GO analysis was performed on the downregulated genes using the GO enrichment analysis tool of Omicshare (<https://www.omicshare.com/tools/home/report/goenrich.html>). GO terms with FDR-corrected $P < 0.05$ were considered significant.

Tandem mass tag proteomic analysis

Tandem mass tags (TMT) proteomics for WT, KI and OE mice was performed in accordance with previously described protocols (Fang et al., 2019). GSEA was conducted using GSEA software v3.1.0 (www.broadinstitute.org/gsea/index.jsp) separately against four protein sets: (1) fibrous sheath-associated proteins (Lehti and Sironen, 2017) (Akap4, Akap3, Gapdhs, Ldhc, Spa17, Fsp1, Fsp2, Ropn1, Ropn11, Ldha, Pde4a, Tekt2, Fscb, Cabyr, Hk1, Aldoa, Slc25a31, Gapdh, Rhp2, Gsk3b, Stat1 and Gstm5); (2) mitochondrial sheath-associated proteins (Lehti and Sironen, 2017) (Klc3, Spata19, Tekt5, Prkar2a, Srsf10, Selenop, Cfp157, Vdac2, Ppp1cc, Gpx4, Tssk2, Ak2, Tex22, Nectin2 and Gopc); (3) ODF-associated proteins (Lehti and Sironen, 2017) (Tek2, Tekt4, Cst8, Vdac2, Vdac3, Cdk5, Odf1, Odf2, Odf3, Uap1 and Ak1); and (4) acrosomal vesicle-associated proteins downloaded from the MSigDB (https://www.gsea-msigdb.org/gsea/msigdb/cards/GOCC_ACROSOMAL_VESICLE).

Analysis of domain and conserved motifs

Protein domains of FSIP2 were predicted by the SMART server (Letunic and Bork, 2018) (<http://smart.embl-heidelberg.de/>). Conserved motifs were predicted by using the MEME motif discovery tool (Bailey et al., 2009) (<http://meme-suite.org/tools/meme>). The aa sequence of FSIP2 of *H. sapiens* (NP_775922.3) and Fsp2 of other seven species [*M. musculus* (A2ARZ3.3), *P. vitticeps* (XP_020670029.1), *L. chalumnae* (XP_014351833.1), *A. planci* (XP_022093257.1), *B. mandarina* (XP_028029952.1), *M. yessoensis* (XP_021368192.1) and *S. pistillata* (PFX30584.1)] were included. The minimum and maximum widths of each motif were set to be 60 aa and 200 aa, respectively. Each motif had to be recognized in at least two sequences. The visual representation of motifs was generated by TBtools (Chen et al., 2020).

Statistical analysis

The data from all experiments were expressed as the mean \pm s.d. Statistical analyses were performed with R package 3.5.1 and Microsoft Excel. P -values were calculated using an unpaired two-tailed t -test. Statistical significance was set at $P < 0.05$.

Acknowledgements

We are very grateful to the patient who participated in this study. We acknowledge Linglong Huang for his kind help with electron microscopy experiments.

Competing interests

The authors declare no competing or financial interests.

Author contributions

Conceptualization: N.L., H.H.; Methodology: X.F., Y.G., W.X., N.L.; Software: X.F.; Validation: Y.G., Z.C., H.M., P.Z., C.S., X.L., H.L., S.Z., C.L., M.Y., Y.L., Z.Y., D.H.; Formal analysis: X.F.; Investigation: Y.G., Z.C., H.M., P.Z., C.S., X.L., H.L., S.Z., C.L., M.Y., Y.L., Z.Y., C.M., L.Z., L.S., N.L.; Resources: Z.C., C.M., L.S.; Data curation: X.F., Y.G., P.Z.; Writing - original draft: X.F., Y.G., N.L.; Writing - review & editing: X.F., Y.G., W.X., H.H., N.L.; Visualization: X.F., Y.G.; Supervision: H.H., L.S., N.L.; Project administration: H.H., L.S., N.L.; Funding acquisition: X.F., P.Z., L.Z., W.X., H.H., N.L.

Funding

This work was supported by the National Natural Science Foundation of China (81701451), the Natural Science Foundation of Guangdong Province of China (2018A030313538), National Key Research and Development Program of China (2018YFC1003603), the China Postdoctoral Science Foundation (2019M662852), the Guangdong Science and Technology Department of Guangdong Province of China (2017A030223003) and the Key-Area Research and Development Program of Guangdong Province (2019B020227001).

Data availability

The single-cell RNA sequencing data have been deposited with the Sequence Read Archive under BioProject PRJNA733327.

Peer review history

The peer review history is available online at <https://journals.biologists.com/dev/article-lookup/doi/10.1242/dev.199216>.

References

- Baccetti, B., Collodel, G., Estenoz, M., Manca, D., Moretti, E. and Piomboni, P. (2005). Gene deletions in an infertile man with sperm fibrous sheath dysplasia. *Hum. Reprod.* **20**, 2790-2794. doi:10.1093/humrep/dei126
- Bailey, T. L., Boden, M., Buske, F. A., Frith, M., Grant, C. E., Clementi, L., Ren, J., Li, W. W. and Noble, W. S. (2009). MEME SUITE: tools for motif discovery and searching. *Nucleic Acids Res.* **37**, W202-W208. doi:10.1093/nar/gkp335
- Ben Khelifa, M., Coutton, C., Zouari, R., Karaouzen, T., Rendu, J., Bidart, M., Yassine, S., Pierre, V., Delarochette, J., Hennebicq, S. et al. (2014). Mutations in DNAH1, which encodes an inner arm heavy chain dynein, lead to male infertility from multiple morphological abnormalities of the sperm flagella. *Am. J. Hum. Genet.* **94**, 95-104. doi:10.1016/j.ajhg.2013.11.017
- Bieniek, J. M., Drabovich, A. P. and Lo, K. C. (2016). Seminal biomarkers for the evaluation of male infertility. *Asian J. Androl.* **18**, 426-433. doi:10.4103/1008-682X.175781
- Bolger, A. M., Lohse, M. and Usadel, B. (2014). Trimmomatic: a flexible trimmer for Illumina sequence data. *Bioinformatics* **30**, 2114-2120. doi:10.1093/bioinformatics/btu170
- Brown, P. R., Miki, K., Harper, D. B. and Eddy, E. M. (2003). A-kinase anchoring protein 4 binding proteins in the fibrous sheath of the sperm flagellum. *Biol. Reprod.* **68**, 2241-2248. doi:10.1095/biolreprod.102.013466
- Chen, Y., Zheng, Y., Gao, Y., Lin, Z., Yang, S., Wang, T., Wang, Q., Xie, N., Hua, R., Liu, M. et al. (2018). Single-cell RNA-seq uncovers dynamic processes and critical regulators in mouse spermatogenesis. *Cell Res.* **28**, 879-896. doi:10.1038/s41422-018-0074-y
- Chen, C., Chen, H., Zhang, Y., Thomas, H. R., Frank, M. H., He, Y. and Xia, R. (2020). TBtools: an integrative toolkit developed for interactive analyses of big biological data. *Mol. Plant* **13**, 1194-1202. doi:10.1016/j.molp.2020.06.009
- Cooper, T. G., Noonan, E., Von Eckardstein, S., Auger, J., Baker, H. W. G., Behre, H. M., Haugen, T. B., Kruger, T., Wang, C., Mbizvo, M. T. et al. (2010). World Health Organization reference values for human semen characteristics. *Hum. Reprod. Update* **16**, 231-245. doi:10.1093/humupd/dmp048
- Coutton, C., Vargas, A. S., Amiri-Yekta, A., Kherraf, Z.-E., Ben Mustapha, S. F., Le Tanno, P., Wambergue-Legrand, C., Karaouzen, T., Martinez, G., Crouzy, S. et al. (2018). Mutations in CFAP43 and CFAP44 cause male infertility and flagellum defects in Trypanosoma and human. *Nat. Commun.* **9**, 686. doi:10.1038/s41467-017-02792-7
- Coutton, C., Martinez, G., Kherraf, Z.-E., Amiri-Yekta, A., Bogueuet, M., Saut, A., He, X., Zhang, F., Cristou-Kent, M., Escoffier, J. et al. (2019). Bi-allelic mutations in ARMC2 lead to severe astheno-teratozoospermia due to sperm flagellum malformations in humans and mice. *Am. J. Hum. Genet.* **104**, 331-340. doi:10.1016/j.ajhg.2018.12.013
- Cruz, A., Sullivan, D. B., Doty, K. F., Hess, R. A., Canisso, I. F. and Reddi, P. P. (2020). Acrosomal marker SP-10 (gene name Acrv1) for staging of the cycle of seminiferous epithelium in the stallion. *Theriogenology* **156**, 214-221. doi:10.1016/j.theriogenology.2020.06.046
- Donkor, F. F., Mönnich, M., Czirr, E., Hollemann, T. and Hoyer-Fender, S. (2004). Outer dense fibre protein 2 (ODF2) is a self-interacting centrosomal protein with affinity for microtubules. *J. Cell Sci.* **117**, 4643-4651. doi:10.1242/jcs.01303
- Eddy, E. M. (2007). The scaffold role of the fibrous sheath. *Soc. Reprod. Fertil. Suppl.* **65**, 45-62.
- Eddy, E. M., Toshimori, K. and O'Brien, D. A. (2003). Fibrous sheath of mammalian spermatozoa. *Microsc. Res. Tech.* **61**, 103-115. doi:10.1002/jemt.10320
- Fang, X., Huang, L.-L., Xu, J., Ma, C.-Q., Chen, Z.-H., Zhang, Z., Liao, C.-H., Zheng, S.-X., Huang, P., Xu, W.-M. et al. (2019). Proteomics and single-cell RNA analysis of Akap4-knockout mice model confirm indispensable role of Akap4 in spermatogenesis. *Dev. Biol.* **454**, 118-127. doi:10.1016/j.ydbio.2019.06.017
- Fawcett, D. W. (1975). The mammalian spermatozoon. *Dev. Biol.* **44**, 394-436. doi:10.1016/0012-1606(75)90411-X
- Gadélha, H. and Gaffney, E. A. (2019). Flagellar ultrastructure suppresses buckling instabilities and enables mammalian sperm navigation in high-viscosity media. *J. R. Soc. Interface* **16**, 20180668. doi:10.1098/rsif.2018.0668
- Green, C. D., Ma, Q., Manske, G. L., Shami, A. N., Zheng, X., Marini, S., Moritz, L., Sultan, C., Gurczynski, S. J., Moore, B. B. et al. (2018). A comprehensive roadmap of murine spermatogenesis defined by single-cell RNA-seq. *Dev. Cell* **46**, 651-667.e610. doi:10.1016/j.devcel.2018.07.025
- Habib, A. M., Matsuyama, A., Okorokov, A. L., Santana-Varela, S., Bras, J. T., Aloisi, A. M., Emery, E. C., Bogdanov, Y. D., Follenfant, M., Gossage, S. J. et al. (2018). A novel human pain insensitivity disorder caused by a point mutation in ZFH2. *Brain* **141**, 365-376. doi:10.1093/brain/awx326

- He, X., Liu, C., Yang, X., Lv, M., Ni, X., Li, Q., Cheng, H., Liu, W., Tian, S., Wu, H. et al. (2020). Bi-allelic loss-of-function variants in cfap58 cause flagellar axoneme and mitochondrial sheath defects and asthenoteratozoospermia in humans and mice. *Am. J. Hum. Genet.* **107**, 514-526. doi:10.1016/j.ajhg.2020.07.010
- Hirohashi, N. and Yanagimachi, R. (2018). Sperm acrosome reaction: its site and role in fertilization. *Biol. Reprod.* **99**, 127-133. doi:10.1093/biolre/iox045
- Jung, M., Wells, D., Rusch, J., Ahmad, S., Marchini, J., Myers, S. R. and Conrad, D. F. (2019). Unified single-cell analysis of testis gene regulation and pathology in five mouse strains. *eLife* **8**, e43966. doi:10.7554/eLife.43966
- Khawar, M. B., Gao, H. and Li, W. (2019). Mechanism of Acrosome Biogenesis in Mammals. *Front Cell Dev Biol* **7**, 195. doi:10.3389/fcell.2019.00195
- La Salle, S., Sun, F. and Handel, M. A. (2009). Isolation and short-term culture of mouse spermatocytes for analysis of meiosis. *Methods Mol. Biol.* **558**, 279-297. doi:10.1007/978-1-60761-103-5_17
- Lehti, M. S. and Siromen, A. (2017). Formation and function of sperm tail structures in association with sperm motility defects. *Biol. Reprod.* **97**, 522-536. doi:10.1093/biolre/iwx096
- Letunic, I. and Bork, P. (2018). 20 years of the SMART protein domain annotation resource. *Nucleic Acids Res.* **46**, D493-D496. doi:10.1093/nar/gkx922
- Li, Y.-F., He, W., Mandal, A., Kim, Y.-H., Digilio, L., Klotz, K., Flickinger, C. J., Herr, J. C. and Herr, J. C. (2011). CABYR binds to AKAP3 and Ropporin in the human sperm fibrous sheath. *Asian J. Androl.* **13**, 266-274. doi:10.1038/aja.2010.149
- Litchfield, K., Summersgill, B., Yost, S., Sultana, R., Labreche, K., Dudakia, D., Renwick, A., Seal, S., Al-Saadi, R., Broderick, P. et al. (2015). Whole-exome sequencing reveals the mutational spectrum of testicular germ cell tumours. *Nat. Commun.* **6**, 5973. doi:10.1038/ncomms6973
- Liu, W., Wu, H., Wang, L., Yang, X., Liu, C., He, X., Li, W., Wang, J., Chen, Y., Wang, H. et al. (2019a). Homozygous loss-of-function mutations in FSIP2 cause male infertility with asthenoteratozoospermia. *J. Genet. Genomics* **46**, 53-56. doi:10.1016/j.jgg.2018.09.006
- Liu, W., Sha, Y., Li, Y., Mei, L., Lin, S., Huang, X., Lu, J., Ding, L., Kong, S. and Lu, Z. (2019b). Loss-of-function mutations in SPEF2 cause multiple morphological abnormalities of the sperm flagella (MMAF). *J. Med. Genet.* **56**, 678-684. doi:10.1136/jmedgenet-2018-105952
- Lukassen, S., Bosch, E., Ekici, A. B. and Winterpacht, A. (2018). Single-cell RNA sequencing of adult mouse testes. *Sci Data* **5**, 180192. doi:10.1038/sdata.2018.192
- Martinez, G., Kherraf, Z.-E., Zouari, R., Fourati Ben Mustapha, S., Saut, A., Pernet-Gallay, K., Bertrand, A., Bidart, M., Hograïndleur, J. P., Amiri-Yekta, A. et al. (2018). Whole-exome sequencing identifies mutations in FSIP2 as a recurrent cause of multiple morphological abnormalities of the sperm flagella. *Hum. Reprod.* **33**, 1973-1984. doi:10.1093/humrep/dey264
- Miki, K., Willis, W. D., Brown, P. R., Goulding, E. H., Fulcher, K. D. and Eddy, E. M. (2002). Targeted disruption of the Akap4 gene causes defects in sperm flagellum and motility. *Dev. Biol.* **248**, 331-342. doi:10.1006/dbio.2002.0728
- Miki, K., Qu, W., Goulding, E. H., Willis, W. D., Bunch, D. O., Strader, L. F., Perreault, S. D., Eddy, E. M. and O'Brien, D. A. (2004). Glyceraldehyde 3-phosphate dehydrogenase-S, a sperm-specific glycolytic enzyme, is required for sperm motility and male fertility. *Proc. Natl Acad. Sci. USA* **101**, 16501-16506. doi:10.1073/pnas.0407708101
- Niederberger, C. (2020). Male Infertility. *J. Urol.* **205**, 1807-1809. doi:10.1097/JU.0000000000001495. doi:10.1097/JU.0000000000001741
- Osuru, H. P., Monroe, J. E., Chebolu, A. P., Akamune, J., Pramoonjago, P., Ranpura, S. A. and Reddi, P. P. (2014). The acrosomal protein SP-10 (Acrv1) is an ideal marker for staging of the cycle of seminiferous epithelium in the mouse. *Mol. Reprod. Dev.* **81**, 896-907. doi:10.1002/mrd.22358
- Piasecka, M., Wenda-Rózewicka, L. and Ogoński, T. (2001). Computerized analysis of cytochemical reactions for dehydrogenases and oxygraphic studies as methods to evaluate the function of the mitochondrial sheath in rat spermatozoa. *Andrologia* **33**, 1-12. doi:10.1046/j.1439-0272.2001.00369.x
- Rashid, S., Grzmil, P., Drenckhahn, J.-D., Meinhardt, A., Adham, I., Engel, W. and Neesen, J. (2010). Disruption of the murine dynein light chain gene Tcte3-3 results in asthenozoospermia. *Reproduction* **139**, 99-111. doi:10.1530/REP-09-0243
- Ricci, M. and Breed, W. G. (2005). Morphogenesis of the fibrous sheath in the marsupial spermatozoon. *J. Anat.* **207**, 155-164. doi:10.1111/j.1469-7580.2005.00437.x
- Satija, R., Farrell, J. A., Gennert, D., Schier, A. F. and Regev, A. (2015). Spatial reconstruction of single-cell gene expression data. *Nat. Biotechnol.* **33**, 495-502. doi:10.1038/nbt.3192
- Shen, Y., Zhang, F., Li, F., Jiang, X., Yang, Y., Li, X., Li, W., Wang, X., Cheng, J., Liu, M. et al. (2019). Loss-of-function mutations in QRICH2 cause male infertility with multiple morphological abnormalities of the sperm flagella. *Nat. Commun.* **10**, 433. doi:10.1038/s41467-018-08182-x
- Sun, L., Fang, X., Chen, Z., Zhang, H., Zhang, Z., Zhou, P., Xue, T., Peng, X., Zhu, Q., Yin, M. et al. (2019). Compound heterozygous ZP1 mutations cause empty follicle syndrome in infertile sisters. *Hum. Mutat.* **40**, 2001-2006. doi:10.1002/humu.23864
- Tang, A., Yan, Q., Sun, L., Diao, R., Yu, Z., Zhang, Z., Gui, Y. and Cai, Z. (2012). Developmental expression of ACRV1 in humans and mice. *Andrologia* **44**, 16-22. doi:10.1111/j.1439-0272.2010.01095.x
- Tang, S., Wang, X., Li, W., Yang, X., Li, Z., Liu, W., Li, C., Zhu, Z., Wang, L., Wang, J. et al. (2017). Biallelic Mutations in CFAP43 and CFAP44 Cause Male Infertility with Multiple Morphological Abnormalities of the Sperm Flagella. *Am. J. Hum. Genet.* **100**, 854-864. doi:10.1016/j.ajhg.2017.04.012
- Visser, W. R., Smith-Harrison, L. I. and Krzastek, S. C. (2020). Surgical procedures for male infertility: an update. *Curr. Opin Urol.* **31**, 43-48. doi:10.1097/MOU.0000000000000828
- Xu, K., Yang, L., Zhang, L. and Qi, H. (2020). Lack of AKAP3 disrupts integrity of the subcellular structure and proteome of mouse sperm and causes male sterility. *Development* **147**, dev181057. doi:10.1242/dev.181057
- Yang, S. M., Li, H. B., Wang, J. X., Shi, Y. C., Cheng, H. B., Wang, W., Li, H., Hou, J. Q. and Wen, D. G. (2015). Morphological characteristics and initial genetic study of multiple morphological anomalies of the flagella in China. *Asian J. Androl.* **17**, 513-515. doi:10.4103/1008-682X.146100
- Young, S. A. M., Miyata, H., Satouh, Y., Aitken, R. J., Baker, M. A. and Ikawa, M. (2016). CABYR is essential for fibrous sheath integrity and progressive motility in mouse spermatozoa. *J. Cell Sci.* **129**, 4379-4387. doi:10.1242/jcs.193151

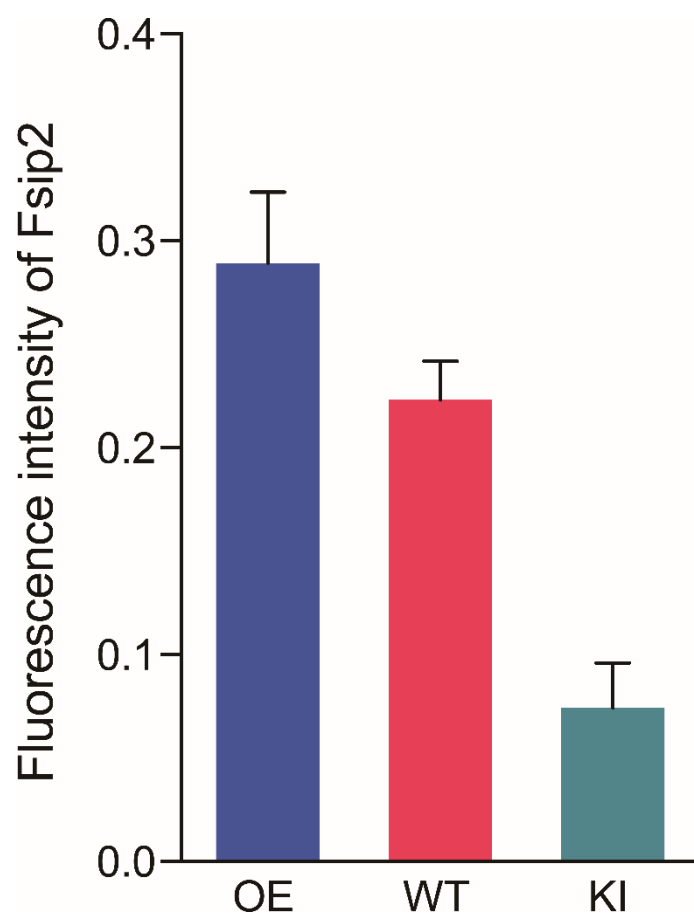


Fig. S1. Fluorescence intensity of Fsip2 of the WT, KI and OE mice sperm.

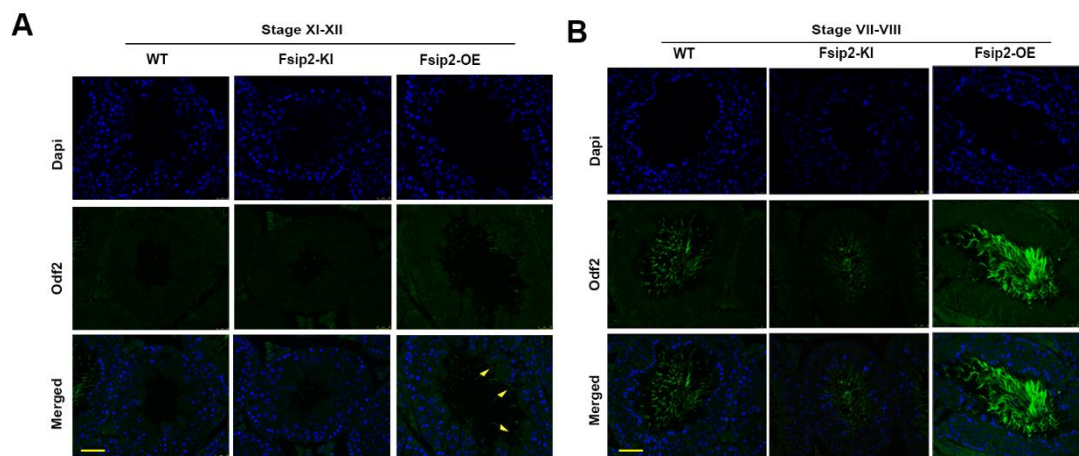


Fig. S2. Immunofluorescence staining of testicular sections. (A) Odf2 expression and distribution in the seminiferous tubule at stage XI-XII. Yellow arrows indicate the accelerated development of spermatid. (B) Odf2 expression at stage VII-VIII.

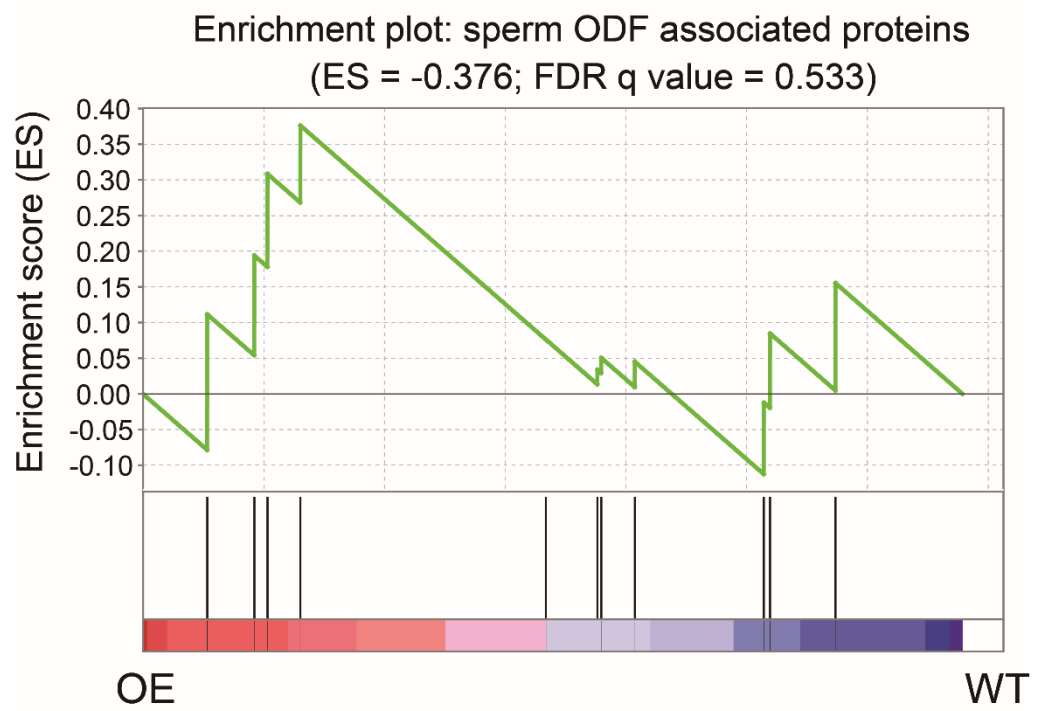
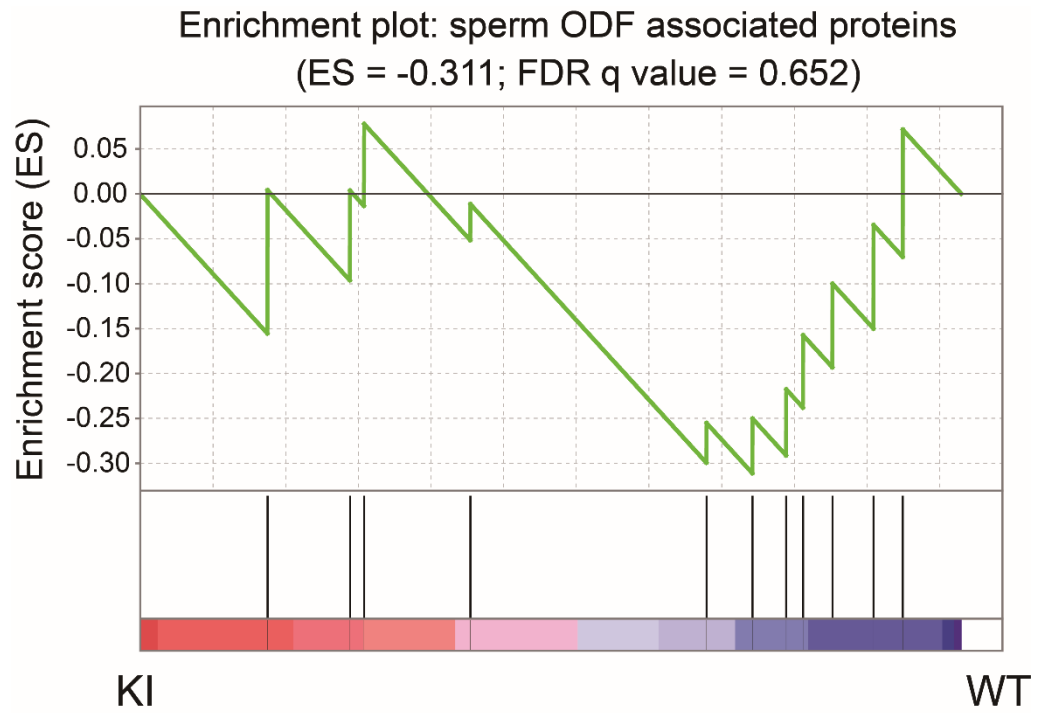


Fig. S3. Gene Set Enrichment Analysis (GSEA) for ODF associated proteins.

Table S1. Testis weight of WT, KI and OE male

Group	Testis Weight/Body Weight (n=11)		
	Mean±SD	P-value	Significance
WT	0.007503 ± 0.000222		
KI	0.007022 ± 0.0003188	0.2298a	n.s.
OE	0.006927 ± 0.000241	0.094b	n.s.

a WT vs KI

b WT vs OE

Table S2. Top three downregulated genes between the 4 subclusters of Round spermatid of the KI and WT mice.

Sub-clusters	Gene 1	Gene 2	Gene 3
Round spermatid 1	<i>Fsip2</i>	<i>Tcte3</i>	<i>Tuba3b</i>
Round spermatid 2	<i>Fsip2</i>	<i>Tcte3</i>	<i>1700017L05Rik</i>
Round spermatid 3	<i>Fsip2</i>	<i>1700109H08Rik</i>	<i>Gm36368</i>
Round spermatid 4	<i>Fsip2</i>	<i>Tcte3</i>	<i>Slx1</i>

Table S3. List of antibodies.

	Antibody	Catalog number	Supplier	RRID	WB dilution	IF dilution
1	Rabbit anti-Fsip2 antibody	bs-16187R	Bioss	AB_2876860	-	1:100
2	Mouse anti-Acrv1 antibody (A-9)	sc-398536	Santa Cruz	AB_2876861	-	1:20
3	Rabbit anti-Akap3 antibody	13907-1-AP	ProteinTech	AB_2273887	1:2000	1:100
4	Rabbit anti-Akap4 polyclonal antibody	24986-1-AP	ProteinTech	AB_2876859	1:2000	1:200
5	Rabbit anti-Odf2 antibody	12058-1-AP	ProteinTech	AB_2156630)	1:500	1:100
6	Rabbit anti-Acrv1 polyclonal antibody	14040-1-AP	ProteinTech	AB_1064042 6	1:1000	-
7	Rabbit anti-Cabyr polyclonal antibody	12351-1-AP	ProteinTech	AB_2069257	1:5000	1:100
8	Rabbit anti-Gapdhs polyclonal antibody	13937-1-AP	ProteinTech	AB_2107611	1:1000	1:100
9	Rabbit anti- β -Actin (13E5) rabbit mAb	#4970	Cell Signalling Technology	AB_2223172	1:1000	-
10	Goat anti-rabbit IgG (H+L) highly cross-adsorbed secondary antibody, Alexa Fluor 488	A11034	Thermo Fisher Scientific	AB_2576217	-	1:600
11	Goat anti-mouse IgG (H+L) cross-adsorbed secondary antibody, Alexa Fluor 568	A11004	Invitrogen	AB_2534072	-	1:600
12	Goat anti-rabbit H&L (HRP)	IgG ab205718	Abcam	AB_2819160	1:10000	-